Chinese Chemical Letters 37 (2026) 110606

Contents lists available at ScienceDirect

Chinese Chemical Letters

journal homepage: www.elsevier.com/locate/cclet

Trace detection of benzene, toluene and xylene (BTX) by chemiresistive metal oxide-based gas sensors: Recent advances in heterojunction materials design

Yidan Chen[a,1], Junzhou Xu[b,d,1], Yanjun Pan[b], Qi Cao[b,*], Kaiping Yuan[c,*]

[a] Department of Chemistry, Fudan University, Shanghai 200438, China
[b] Key Laboratory of Energy Thermal Conversion and Control of Ministry of Education, School of Energy and Environment, Southeast University, Nanjing 210096, China
[c] Frontier Institute of Chip and System, State Key Laboratory of Integrated Chips and Systems, Fudan University, Shanghai 200438, China
[d] School of Environmental Science and Engineering, Shanghai Jiao Tong University, Shanghai 200240, China

ARTICLE INFO

Article history:
Received 21 September 2024
Revised 29 October 2024
Accepted 1 November 2024
Available online 1 November 2024

Keywords:
Trace detection
Benzene, toluene and xylene (BTX)
Chemiresistive
Heterojunction
Metal oxide semiconductor (MOS)

ABSTRACT

As the chemical industry expands, the use of benzene, toluene, and xylene (collectively known as BTX) in industrial production has increased greatly. Meanwhile, the toxic nature and potential health hazards of BTX gases cannot be ignored due to low-concentration leaks underline the critical need for rapid and real-time monitoring of these gases. Chemiresistive metal oxide semiconductor (MOS)-based gas sensors, which are extensively used for gas detection in both industrial settings and everyday life, emerge as one of the optimal solutions for trace BTX detection. These sensors are highly valued for their high sensitivity and low detection limits. Nevertheless, the improvement of selectivity towards specific BTX gases to achieve efficient and precise detection still remains challenging. This review summarizes the chemiresistive MOS-based gas sensors designed for BTX detection, categorizing them based on the components of sensing materials-basically into three groups: single-component, single heterojunction, and multiple heterojunctions gas sensing materials. Further, the review proposes the future application prospects of chemiresistive MOS-based BTX gas sensors, with specific emphasis on their significance in promoting industrial safety and environmental monitoring.

© 2025 Published by Elsevier B.V. on behalf of Chinese Chemical Society and Institute of Materia Medica, Chinese Academy of Medical Sciences.

1. Introduction

With the rapid development of industrialization and urbanization, the degradation of air quality caused by air pollution from various sources such as fossil fuel combustion [1], power generation [2], and industrial activities [3] has become a pressing issue. Volatile organic compounds (VOCs), specifically alcohols, aldehydes, and aromatic hydrocarbons, are the most prevalent pollutants in the atmosphere [4], significantly impacting the ecological environment [5], posing health risks [6] to the population, and contributing to global climate change. While regulatory agencies monitor air pollution levels on a daily basis, their focus is typically on providing average air quality indices for specific regions, often neglecting the VOC gases present in individuals' immediate living environments. These gases often go unnoticed until individuals experience discomfort, by which time the harmful substances have already inflicted significant damage to their bodies. The World Health Organization (WHO) has reported that approximately 7 million people die each year due to various forms of air pollution, with 3.8 million deaths attributed to household air pollution [7].

Among VOCs, benzene-series compounds, collectively known as BTX, have a substantial impact on human health. This group includes benzene, toluene and xylene. They are extensively utilized as critical raw materials for the production of various chemicals, petrochemical industrial products, organic solvents, and additives in chemical processes [8–10]. Due to their high consumption rates, the leakage frequency of BTX compounds is significant in China, with the potential for bioaccumulation through the food chain. Once these compounds enter the human body, they can affect vital organs such as the liver, lungs, heart, kidneys, and brain [11]. Prolonged exposure to BTX compounds can damage chromosomes in cells leading to leukemia and tumor [12]. According to the WHO, reducing the concentration of benzene in the air from 1.7 μg/m^3 to 0.17 μg/m^3 can decrease the probability of leukemia in humans by approximately 100 times [13]. Moreover, research indi-

* Corresponding authors.
E-mail addresses: qicao@seu.edu.cn (Q. Cao), kpyuan@fudan.edu.cn (K. Yuan).
[1] These authors contributed equally to this work.

https://doi.org/10.1016/j.cclet.2024.110606
1001-8417/© 2025 Published by Elsevier B.V. on behalf of Chinese Chemical Society and Institute of Materia Medica, Chinese Academy of Medical Sciences.

Table 1
Partial limitations of the "Control Standards for Indoor Environmental Pollution in Civil Building Engineering" (GB 50325–2020).

Toluene limit (Level I buildings)	Toluene limit (Level II buildings)	Xylene limit (Level I buildings)	Xylene limit (Level II buildings)
$\leq$0.15 mg/m^3	$\leq$0.20 mg/m^3	$\leq$0.20 mg/m^3	$\leq$0.20 mg/m^3

cates that even prolonged exposure to low concentrations of benzene in the environment can increase the likelihood of leukemia by 2–3 times [14]. Considering China's significant consumption of BTX compounds and their severe health hazards, the People's Republic of China has implemented the "Indoor Environmental Pollution Control Standard for Civil Buildings" (GB 50325–2020) since 2020 [14].

Compared to the previous version (GB 50325–2010), GB 50325–2020 imposes restrictions on the concentrations of toluene and xylene in the ambient environment of civil construction projects, as shown in Table 1. In addition, the "Indoor Air Quality Standard" (GB 18,883–2022), implemented by State Administration for Market Regulation of China in early 2023, has further reduced the permissible limit for benzene in indoor air. The limit has been tightened from $\leq$0.11 mg/m^3, as specified in the previous GB 18,883–2002, to $\leq$0.03 mg/m^3, resulting in a reduction of approximately 75 %.

The development of instruments and devices for the rapid and accurate monitoring of BTX gas concentrations in the air is of utmost importance [15]. Currently, gas chromatography, ion chromatography, and chemiluminescence are common methods for gas detection [16–18]. Although these methods offer precise and low-error detection results, their high cost and lack of portability restrict their application range. Gas sensors, on the other hand, have emerged as an optimal choice for BTX gas detection in production and daily life [19,20], primarily due to their compact size, low production cost, and potential for integration [21–23]. Among various types of VOCs gas sensors available, resistive-based gas sensors have attracted significant attention. These sensors detect VOCs gases by measuring the resistance change of the sensor, converting the VOCs gas concentration into an electrical signal for detection [24–26]. Resistive-based gas sensors consist of two main components: the sensitive material and the transducer. The sensitive material is the core of the sensor which determines the sensing performance, including MOS, carbon-based material, conducting polymer and so on. Among them, the MOS is the most widely used in commercial settings because of its characteristics of high sensing response and operating stability, and the research on MOS sensing material is the most thorough [27–30].

The gas sensing mechanism of the MOS can be explained by the oxygen adsorption model. In an ambient air atmosphere, oxygen molecules adsorb onto the surface of the gas-sensitive material through the process of adsorption. Subsequently, these oxidative gas molecules attached to the material's surface capture electrons from the semiconductor gas-sensitive material, resulting in the formation of negatively charged oxygen ions (O_2^-, O^-, O^{2-}) [31,32]. The reaction of the oxygen ion formation is shown as following:

$$\text{In air: } O_{2(gas)} \rightarrow O_{2(ads)} \tag{1}$$

$$T < 100\ ^\circ\text{C: } O_{2(ads)} + e^- \rightarrow O_2{}^-{}_{(ads)} \tag{2}$$

$$100\ ^\circ\text{C} < T < 300\ ^\circ\text{C: } O_{2(ads)} + e^- \rightarrow 2O^-{}_{(ads)} \tag{3}$$

$$T > 300\ ^\circ\text{C: } O^-{}_{(ads)} + e^- \rightarrow O^{2-}{}_{(ads)} \tag{4}$$

When the gas-sensitive material is transferred from the air atmosphere to a BTX (reducing gas) atmosphere, BTX gases react with the released oxygen ions, causing the oxygen ions to release electrons and return to their initial state. In the case of n-type oxide semiconductors exposed to a BTX atmosphere, the carrier concentration increases, leading to a decrease in material resistance [33]. Conversely, for p-type oxide semiconductors, the opposite behavior occurs [34]. Thus, the detection of BTX gases can be achieved by measuring the resistance change of the material, reflecting its sensing characteristics towards BTX gases.

The advantages and disadvantages of gas-sensitive materials in chemiresistive gas sensors can be reflected through specific performance indicators. These parameters can be employed to evaluate whether the gas-sensitive materials meet the requirements of the application. The main parameters in gas sensitivity testing are listed as follows:

(1) Response

Gas sensor "response" represents the change in measured electrical signal (*e.g.*, *I*, *C*, *R*, *Z*, *V*, or *E*) due to introduction of analytes. The variation of sensor response with changing concentration of analytes provides the first information of the sensor. The sensor is responding or not in the presence of corresponding analyte. The sensor may respond oppositely to introduction of two different types of gas molecules (*e.g.*, oxidizing, reducing gases) [35,36]. Conventionally, the response value is quantified as the ratio between the electrical signal value of the sensor in the air and the same value when it is exposed to the target gas.

(2) Sensitivity

Sensitivity is evaluated using the response rate of a gas sensor, referring to the extent of change in the response quantity caused by a unit change in the concentration or quantity of the target gas. For gas sensors, a higher response rate indicates greater sensitivity of the device to the gas. The formula is presented as Eq. 5 or Eq. 6, where R_a represents the resistance value of the gas-sensitive material in air, and R_g represents the resistance value of the gas-sensitive material in the testing gas [37,38].

$$S = \frac{R_a - R_g}{R_g} \tag{5}$$

$$S = \frac{R_a}{R_g} \tag{6}$$

(3) Selectivity

Selectivity is also a highly desired parameter of a sensor and is defined as the ability to discriminate specific gas analytes in presence of other gas analytes in the sample. Selectivity can be measured by taking sensor responses in presence of the targeted analytes as well as all possible interfering compounds separately. Sensitivity depends on factors such as device noise levels, environmental influences, and the characteristics of the gas-sensitive material [39,40].

(4) Limit of detection (LOD)

LOD refers to the lowest gas concentration that a gas sensor can detect. When the gas concentration falls below this limit, the gas sensor cannot distinguish between gas signals and noise signals, resulting in inaccurate measurement of the target gas concentration [41]. Generally, gas sensors with lower detection limits exhibit higher sensitivity and accuracy, but this comes at the cost of increased sensor expenses and manufacturing complexity [42–44].

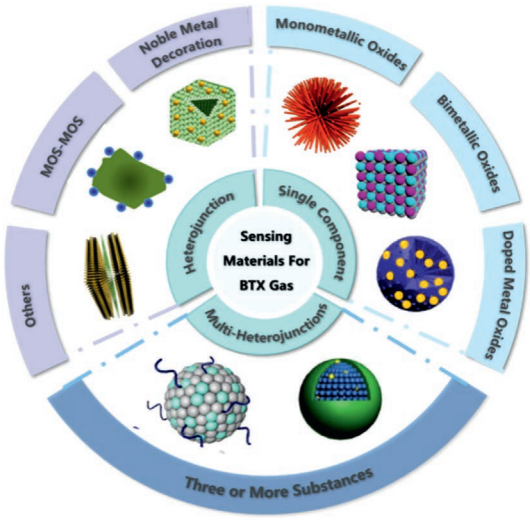


Fig. 1. Classification of the sensitive material for BTX gas detection.

(5) Response time/Recovery time

Response and recovery time are also crucial performance indicators for gas sensors. When the gas-sensitive material comes into contact with the target gas or experiences changes in gas concentration, the resistance of the material changes and eventually stabilizes over a certain period of time [45,46]. The response time (t_{res}) is defined as the time taken for the sensor's resistance to change by 90 % when it comes into contact with the target gas while the recovery time (t_{rec}) is defined as the time taken for the sensor's resistance to change by 90 % when it comes into contact with the air [47,48].

(6) Stability

Reproducibility refers to the change in the output signal of a gas sensor as the concentration of the target gas varies. When the target gas concentration returns to its original value, the gas sensor's signal also returns to its original state [49]. Gas sensors with high reversibility can accurately measure various gas concentrations within different gas environments, offering higher precision and reliability [50].

As discussed earlier, research on the detection of BTX gases is crucial for both the environment and human health. However, based on a literature survey, the number of comprehensive reviews on resistive MOS-based gas sensors for BTX gas detection is currently limited. This paper aims to provide a comprehensive review of the latest advancements in BTX gas sensors, categorizing gas-sensitive materials into three groups as shown in Fig. 1: Single-component gas-sensitive materials, one heterojunction gas-sensitive materials, and multiple heterojunctions gas-sensitive materials. Additionally, it will discuss how different sensing materials, morphologies, temperatures, and other parameters influence the sensitivity of gas sensors toward BTX gases.

2. Gas sensors composed of single-component gas-sensitive materials

2.1. Monometallic oxides

Monometallic oxides are the simplest MOS sensing material in terms of material composition and preparation process. According to the sensing mechanism of the MOS, the sensing properties is related to both the number of adsorption sites and the ratio of electron depletion layer to material core [51–53]. Gas-sensitive materials based on metal oxides with higher specific surface areas are particularly favorable for the adsorption and desorption of gas molecules, for example, hollow structures, core-shell structures, porous mesoporous materials, double-shelled hollow spheres and some low dimensional structures such as nanoparticles (NPs), one-dimensional nanorods (NRs), nanowires (NWs), and two-dimensional nanosheets (NSs) [54]. This facilitates rapid changes in electrical resistance during gas detection, even at lower operating temperatures [55,56]. In recent years, research has increasingly focus on synthesizing gas-sensitive materials with higher specific surface areas by manipulating the microstructure and crystalline properties of metal oxide nanomaterials (Table 2) [51–54,56–88].

Experiments in different conditions will synthesize different kinds of nanostructures and get various morphologies [56–60]. Tshabalala *et al.* [56] achieved TiO_2 NPs (TNPs), TiO_2 NWs (TNWs) and sea-urchin-like hierarchically (HHC) arranged TiO_2 nanostructures *via* a facile hydrothermal method, and the concrete procedures and micrography from SEM are shown in Figs. 2a-c. The Brunauer Emmett Teller (BET) result shows the surface areas of TNP, TNW and HHC are 68.23, 125.79 and 100.47 m^2/g. Because the NPs have a smaller surface area, the NP agglomerates reduce its efficiency as gas transfer to the inner parts of the agglomerates is hindered. According to the gas sensing test result, it is interesting that the selectivity of the TNW sensor is influenced by the temperature (Figs. 2d and e). The sensor shows a high response signal of 6.57 at 25 °C when exposed to C_7H_8 (Fig. 2f). With the temperature increased, the sensor exhibits a higher response signal of 9.69 at 125 °C when exposed to C_8H_{10} (Fig. 2g). Therefore, the TNWs sensors have dual-functionality sensing properties which is different from other TiO_2 nanostructure-based sensors. Additionally, the HHC-based sensors exhibit a response signal of 2.46 toward CO at 25 °C. Hegde *et al.* [57] reported a TiO_2 nanotube-based sensor array which had a high surface area, showed good sensing properties to benzene at room temperature. The TiO_2 nanotubes (NTs) were firstly synthesized by electrochemical anodization and then oxygen annealed in a tube furnace in order to get a self-organized, n-type TiO_2 nanotube array and the detecting process of TiO_2 nanotube sensor for benzene is shown in Fig. 2h. Because of the large surface area, it can perform an excellent response to benzene from 100 ppb to 400 ppb by working with a simple and portable instrumentation and the response is proportional to the concentration of benzene. Additionally, in the concentration range of 100–400 ppb, the sensor exhibited a short response time between 8 s and 23 s. What is the sensor specific compared to other VOCs sensors is that it can work without heating at the temperature between 25 °C and 40 °C. Vanadium pentoxide (V_2O_5) is one of n-type metal oxide semiconductors with a wide bandgap, making it a promising candidate for gas sensor applications due to its high chemical and thermal stability. Cao *et al.* [58] used a simple hydrothermal method to design flower-like V_2O_5 hierarchical nanostructures (HNs) for the selective and sensitive detection of xylene. They adjusted the morphologies and sensing properties of V_2O_5 by changing the hydrothermal reaction time. From the SEM and TEM images (Figs. 2i and j), the V_2O_5 HNs have diameter of 3–5 μm and consist of various nanosheet-type and nanoneedle-type structures. According to the BET and BJH (Barret Joyner Halenda) analysis, the surface area of the flower-like V_2O_5 HNs is 19.5291 m^2/g. The gas sensing property test results show that 300 °C is the best working temperature for xylene detection (Fig. 2k). When the temperature is below 300 °C, the xylene molecules cannot be activated completely, and when working at temperature above 300 °C, it is difficult for xylene molecules to adsorb on the surface of the sensing material. The V_2O_5 HNs-based sensor has a good response to

Table 2
BTX gas sensing materials-Single component.

Material	Morphology	Sensitive gas	Optimal working temperature	Limit of detection	Response (concentration)	Refs.
TiO_2	Nanotubes	Benzene	Room temperature	100 ppb	4–24 (100–400 ppb)	[56]
SnO_2	Nanoparticles	Benzene	Room temperature	/	15 (100 ppm)	[57]
Zn_2SnO_4	Nanowires	Benzene	299 °C	/	3 (100 ppb)	[51]
Co_3O_4	Nanosheets	Toluene	200 °C	/	1.5 (100 ppm)	[74]
CuO	Nanoparticles	Toluene	160 °C	/	35 % (240 ppm)	[75]
$ZnFe_2O_4$	Nanospheres	Toluene	300 °C	/	9.98 (100 ppm)	[76]
Zn_2SnO_4	Nanosheets	Toluene	280 °C	/	25.2 (100 ppm)	[53]
Co_3O_4	Nanosheets	Toluene	180 °C	5 ppm	8.5 (200 ppm)	[77]
$NiFe_2O_4$	Nanospheres	Toluene	400 °C	2.5 ppb	115.4 (5 ppm)	[61]
$NiFe_2O_4$	Core shell	Toluene	240 °C	1 ppb	19.95 (100 ppm)	[62]
$ZnFe_2O_4$	Core shell	Toluene	250 °C	0.2 ppm	79 (100 ppm)	[65]
ZnO	Nanorods	Toluene	400 °C	/	64 (20 ppm)	[78]
TiO_2	Nanowires	Toluene	Room temperature	0.52 ppm	6.57 (40 ppm)	[56]
Co_3O_4	Nanosheets	Toluene	150 °C	/	38.7 (5 ppm)	[79]
Sn-doped Co_3O_4	Nanowires	Toluene	220 °C	/	7.58 (100 ppm)	[67]
Sn-doped Co_2O_3	Nanoparticles	Toluene	240 °C	0.19 ppm	53.8 (50 ppm)	[68]
Ni-doped ZnO	Nanospheres	Toluene	325 °C	500 ppb	210 (100 ppm)	[52]
CoPP-doped TiO_2	Nanoparticles	Toluene	327 °C	several ppb	2.45 (10 ppm)	[80]
Ti-doped Co_3O_4	Nanoparticles	Toluene	280 °C	1 ppm	65.6 (50 ppm)	[66]
Fe-doped In_2O_3	Nanofibers	Toluene	275–300 °C	/	13 (5 ppm)	[71]
MoO_3	Nanosheets	Xylene	300 °C	0.1 ppm	38 (100 ppm)	[81]
$NiFe_2O_4$	Fusiformis	Xylene	300 °C	10 ppm	31.52 (500 ppm)	[63]
NiO	Nanosheets	Xylene	225 °C	5 ppm	262 (100 ppm)	[59]
V_2O_5	Nanospheres	Xylene	290 °C	1 ppm	2.76 (100 ppm)	[60]
V_2O_5	Nanosheets	Xylene	300 °C	1 ppm	2.2 (100 ppm)	[58]
$ZnCo_2O_4$	Nanosheets	Xylene	260 °C	/	46 (200 ppm)	[64]
$ZnFe_2O_4$	Nanorods	Xylene	200 °C	/	47.4 % (50 ppm)	[82]
ZnO	Nanosheets	Xylene	Room temperature	/	2.4 (100 ppm)	[83]
Co_3O_4	Nanosheets	Xylene	220 °C	/	59 (50 ppm)	[84]
Ni-doped ZnO	Nanowires	Xylene	400 °C	0.04 ppm	42.4 (5 ppm)	[72]
Sn-doped NiO	Nanospheres	Xylene	225 °C	0.3 ppm	20.2 (100 ppm)	[69]
W-doped NiO	Nanotubes	Xylene	375 °C	/	8.74 (200 ppm)	[73]
Au-doped $WO_3{\cdot}H_2O$	Nanocubes	Xylene	255 °C	200 ppb	26.4 (5 ppm)	[85]
$CuCo_2O_4$	Nanosheets	Xylene	150 °C	0.5 ppm	2.7 (50 ppm)	[86]
$NiCo_2O_4$	Nanospheres	Xylene	240 °C	/	16.7 (100 ppm)	[87]
$NiCo_2O_4$	Nanospheres	Xylene	240 °C	/	23.3 (100 ppm)	[88]
Sn-doped NiO	Nanosphere	Xylene	250 °C	63 ppb	46.7 (100 ppm)	[54]
Sn^{2+}-doped NiO	Nanospheres	Xylene	180 °C	ppb level	30 (10 ppm)	[70]

xylene from the concentration of 1 ppm to 500 ppm, and the result is shown in Fig. 2l.

Designing porous or mesoporous sensing material is one of the methods to improve the sensing performance. Wang *et al.* [59] prepared a porous sheet-like NiO-based sensor for xylene detection by hydrothermal and sintering method. NiO is a typical p-type semiconductor, which has advantages of good stability but also has weakness, such as low sensitivity. However, the porous nanostructures enables this sensor to exhibit good sensing property and low optimum working temperature. According to the sensing test result, when exposed to 100 ppm xylene gas, the response value is 2.62 at 225 °C which is the best operating temperature, and the limit of detection is 5 ppm xylene gas. Besides, this porous sheet-like NiO-based sensor shows that the value response signal in xylene is almost 20 times higher than that in benzene, which certified its good sensitivity. In another study related to V_2O_5-based gas sensor, Cao *et al.* [60] reported a highly ordered mesoporous V_2O_5 nanospheres (NSs) that have good performance for selective detection of xylene. The V_2O_5–NSs made by a template-free solvothermal method have a huge surface area of 5.233 m^2/g and the pore diameter of 18.91 nm. The V_2O_5 NSs-based gas sensor exhibits response signal of 2.75 and rapid response time of 21 s toward 100 ppm xylene at the optimum temperature of 290 °C. When exposed to xylene gas, xylene molecules have a reaction with the O^- on the surface of the sensing material, leading to a thinner depletion layer and a lower barrier, so the resistance will be lower. The specific chemical reaction between xylene and O^- is as follows:

$$C_8H_{10} + 21O^- \rightarrow 5H_2O + 8CO_2 + 21e^- \ (100\ ^\circ C < T < 300\ ^\circ C) \quad (7)$$

2.2. Bimetallic oxides

Compared to single metal oxides, bimetallic oxides have synergistic modification effects, especially in catalysis and gas sensing. Spinel structured semiconductor metal oxides with the general structural formula AB_2O_4, such as $NiFe_2O_4$ [61–63], Zn_2SnO_4 [53], $ZnCo_2O_4$ [64] and so on, have received a lot of attention in the field of gas sensing. Many studies show that this kind of semiconductor can be a good candidate for BTX gas detection. Zhang *et al.* [63] demonstrated a p-type $NiFe_2O_4$ fusiformis derived from Ni/Fe bimetal metal-organic frameworks (MOFs). They used a simple hydrothermal approach to prepare the MOFs precursors and then the MOFs were calcined in an air atmosphere at 350 °C, and the preparation process is shown in Fig. 3a. According to the characterization test, the $NiFe_2O_4$ fusiformis have a huge surface area of 60.50 m^2/g because of the porous microstructure (Fig. 3b). The gas sensors made of $NiFe_2O_4$ fusiformis have good sensing property for xylene gas detection at 300 °C, and exhibit a response of 31.52 toward 500 ppm xylene. When respectively exposed to various gas, the sensor performed a high selectivity to xylene (Figs. 3c–e). Among numerous studies, $ZnFe_2O_4$ is more popular than other spinel structured semiconductor metal oxides due to its low price, structure, rich content and easy fabrication. Zhang *et al.* [65] synthesized hollow urchin-like core-shell spinel structured $ZnO/ZnFe_2O_4$ composite and pure $ZnFe_2O_4$ sensing material

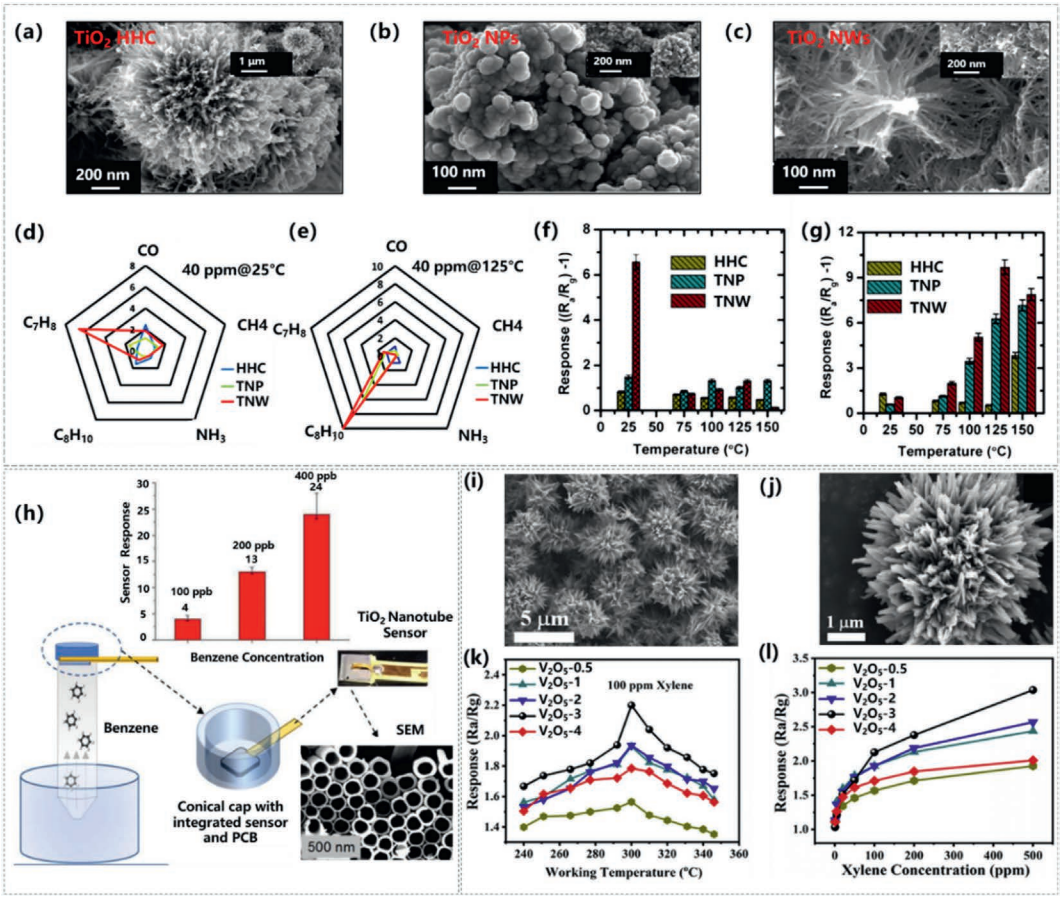


Fig. 2. (a-c) SEM images of TiO_2 HHC, NP and NWs. (d, e) Selectivity plot of the various sensors exposed to 40 ppm gas concentration at 25 °C and 150 °C. (f, g) Resistance against time plot showing n-type chemiresistive sensor characteristics and the sensor response against temperature at 40 ppm of C_7H_{10} and C_8H_{10}. (a-g) Reprinted with permission [56]. Copyright 2021, American Chemical Society. (h) The process of TiO_2 nanotube sensor for benzene detection. Reprinted with permission [57]. Copyright 2021, Institute of Electrical and Electronics Engineers. (i) SEM view of urchin flower-like V_2O_5–3HNs. (j) SEM view of single urchin flower-like V_2O_5–3. (k) Temperature dependent response study of all the fabricated flower-like V_2O_5 HNs sensors towards 100 ppm xylene. (l) Plot of the relationship between the response of flower-like V_2O_5 HNs sensors as a function of different xylene concentrations at 300 °C. (i-l) Reprinted with permission [59]. Copyright 2020, Elsevier.

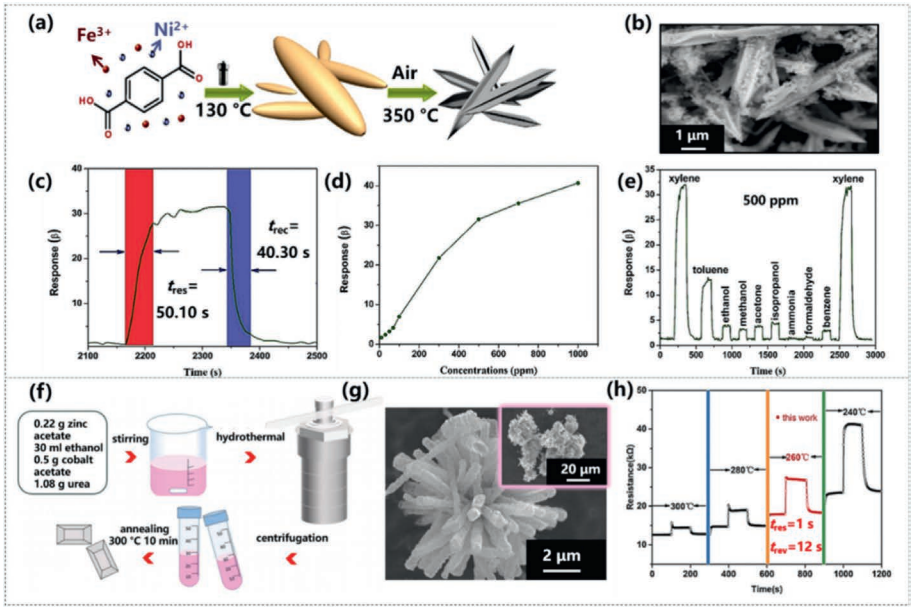


Fig. 3. (a) Schematic illustration for the preparation of $NiFe_2O_4$ fusiformis. (b) SEM image of $NiFe_2O_4$ fusiformis. (c) Typical response and recovery time to 500 ppm xylene. (d) Relationship between the response values and xylene concentrations. (e) Selectivity of sensor based on $NiFe_2O_4$ fusiformis to 500 ppm of various gases at 300 °C. (a-e) Reprinted with permission [62]. Copyright 2020, Springer Nature. (f) The schematic illustration of the $ZnCo_2O_4$ HPA synthesis. (g) The FESEM image of the $ZnCo_2O_4$ HPA. (h) Dynamic resistance variation. (f-h) Reprinted with permission [64]. Copyright 2022, Elsevier.

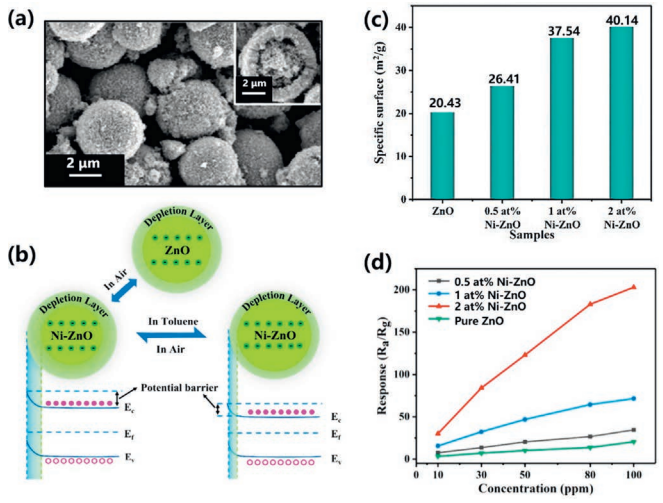


Fig. 4. (a) SEM image of core-shell morphology. Copyright 2022, Elsevier. (b) Schematic diagram of the sensing mechanism. (c) Specific surface area of the samples. (d) The response of the pure, 0.5, 1, and 2 at% Ni-ZnO sensors to (10–100 ppm) toluene. (a-d) Reprinted with permission [52]. Copyright 2022, Elsevier.

by a simple solvothermal method. On the basis of the experimental result, the ratios of Zn to Fe have an influence on the product. If the ratio of Zn to Fe is 1:2, the product is only $ZnFe_2O_4$, and if the content of Zn is the same as Fe or the proportion of 2:3, the product comprises ZnO and $ZnFe_2O_4$. The gas sensing test shows that the pure $ZnFe_2O_4$-based sensor exhibits a highest response toward 79–100 ppm toluene at a very low working temperature and the limit detection is 0.2 ppm.

In another study related to spinel structured semiconductor metal oxides, Li *et al.* [64] reported a p-type hollow porous tube assembled $ZnCo_2O_4$ hierarchical porous architectures (HPA) synthesized by a solvothermal method and annealing treatment. The schematic illustration of the $ZnCo_2O_4$ HPA synthesis is presented in Fig. 3f, and the FESEM is shown in Fig. 3g. According to nitrogen adsorption-desorption measurement, the $ZnCo_2O_4$ HPA has a huge surface area of 35.6 m^2/g. Moreover, the $ZnCo_2O_4$ HPA-based gas sensor exhibits good response to xylene at the optimum operating temperature of 260 °C and show a rapid response time and recovery time of 1 s and 12 s, respectively (Fig. 3h). This is due to appropriate activity and distinctive hierarchical porous structures of the $ZnCo_2O_4$ HPA, which can not only promote the oxidation of xylene and improve surface chemical reaction, but also make for the gas adsorption and desorption.

Currently, only a small amount of spinel structured MOS are used in gas sensing, and its weakness of high preparation temperature limits the application. Therefore, the exploration of a simple and green synthesis method is still challenging for spinel structured MOS-based gas sensor.

2.3. Doped metal oxides

Doping transition metal ions is an efficient tactic for metal oxides to improve their sensing performance. The doping of transition metal ions (*e.g.*, Ti [66], Sn [54,67–70], Fe [71], Ni [52,72]) into the semiconductor lattice results in the lattice distortion of sensitive materials and thus generates a large number of defects and vacancies. The increase in the defect concentration on the surface can improve the adsorption of oxygen anions on the surface of the material, thereby improving the gas-sensing response value of the sensing material. Nowadays, many studies have been devoted to transition metal ion-doped metal oxides. Li *et al.* [52] displayed a Ni-doped ZnO with core-shell morphology (Fig. 4a). They used one-step solvothermal method and synthesized different ratios of 0, 0.5, 1, 2 at% Ni-doped ZnO. As shown in Fig. 4c, with the ratio of Ni increasing, the specific surface of the sensing material is raised. According to the sensing test results shown in Fig. 4d, the sensor based on 1 at% Ni-doped ZnO exhibited the best sensing performance towards toluene gas from 210 ppm to 100 ppm at 325 °C, and it can detect the toluene as low as 500 ppb. The response and recovery time are 2 s and 77 s, respectively. Through the molecular level research, it is confirmed that the better sensing performance of 1 at% Ni-doped ZnO is contributed to the catalyst effect of Ni ions and the improvement in the specific surface area and relative percentage of oxygen vacancy after Ni doping. The sensing mechanism is shown in Fig. 4b.

In_2O_3 is an excellent catalyst for toluene oxidation and it will strengthen the selectivity of the sensing material. Lee *et al.* [71] reported a Fe-doped In_2O_3 nanofiber-based gas sensor arrays for detection of indoor VOCs. They prepare pure and four different doping contents of Fe (0.05, 0.1, 0.3 and 0.5 at%) In_2O_3 nanofibers *via* electrospinning. Compared with pure In_2O_3, there are two gas sensing characteristics being changed. Firstly, the addition of Fe has an influence on the sensing temperature, and the temperatures to show maximum gas response decrease. Besides, the response value of other gas, such as ethanol and formaldehyde, is reduced, hence the selectivity is enhanced. The sensing changes are all attributed to the catalytic activity of Fe and Fe-induced changes in the mesopore volume, surface area, oxygen adsorption, and charge carrier concentration.

Co_3O_4 is a typical p-type semiconductor with high selectivity for gas detection. However, the Co_3O_4-based sensors have a weakness of low sensitivity because of the relatively low reactivity of toluene. Zhang *et al.* [68] prepared a mesoporous Sn-doped Co_3O_4 whiskers by a new method of the preparation and sintering of salicylic anion-intercalated Sn-doped cobalt layered hydroxide whiskers. Compared with pure Co_3O_4, Sn-doped Co_3O_4 has smaller crystal sizes, lower crystallinity, and higher specific surface area with the highest value of 26.4 m^2/g. According to the gas sensing characteristic test, the Sn-doped Co_3O_4-based sensor show response to 53.8−50 ppm of toluene at 240 °C, and the value is 7.6 times higher than that of pure Co_3O_4. Combined with the superiority of Co_3O_4, the Sn-doped Co_3O_4-based sensors also have good selectivity toward toluene gas. Judging by the sensing mechanism, the introduction of Sn changes the hole concentration and specific surface area and active site. Therefore, it is an efficient method for p-type semiconductors to enhance sensing performance.

Although the sensors made of single component have a lot of advantages such as simple synthesis, low cost and so on, their sensing properties are unable to meet test requirements in some specific circumstances. Therefore, many studies about sensing material have focused on doping metal oxide with other substances.

3. Heterojunction of metal-oxide semiconductor

3.1. Noble metal decorated metal oxides

Noble metal mainly refers to gold (Au) [89–91], silver (Ag) [92,93] and platinum (Pt) [94,95] group metals. When designing gas sensing materials, modifying noble metals on the surface of nanostructured metal oxide semiconductor gas sensing materials to form heterojunctions is a good method to enhance their sensing performance (Table 3). The main mechanism can be divided into two aspects. On the one hand, it is the electron sensitization effect. Due to the high work function of precious metals, the electrons generated during the sensing process will be transferred from the conduction band of the metal oxide semiconductor to the precious metal until the Fermi level is equal. This behavior leads to the formation of Schottky barriers and an increase in the thick-

Table 3
BTX gas sensing materials - Noble metal decorated metal oxides.

Material	Morphology	Sensitive gas	Optimal working temperature	Limit of detection	Response (concentration)	References
Ag-Bi_2O_3	Nanorods	Toluene	Room temperature	10 ppm	89.21 (50 ppm)	[100]
Ag-$LaFeO_3$	Nanoparticles	Toluene	215 °C	/	24.0 (5 ppm)	[91]
Au-$ZnSnO_3$	Nanocubes	Toluene	240 °C	0.01 ppm	80.82 (100 ppm)	[89]
Au-SnO_2	Nanorods	Toluene	450 °C	0.01 ppm	328 (10 ppm)	[101]
Pd-SnO_2	Nanosheets	Toluene	250 °C	0.08 ppm	17.4 (10 ppm)	[102]
Pd-SnO_2	Nanoparticles	Toluene	350 °C	/	25 (50 ppm)	[103]
Pt-In_2O_3	Nanofibers	Toluene	250 °C	/	1.54 (10ppm)	[104]
Pt-ZnO	Nanowires	Toluene	Room temperature	0.3 ppb	2.86 (50 ppm)	[99]
Au-MoO_3	Nanoparticles	Toluene	250 °C	5 ppb	17.5 (100 ppm)	[105]
Ag-Co_3O_4	Core shell nanoparticles	Xylene	250 °C	/	2.47 (50 ppm)	[106]
Au-SnO_2	Nanorods	Xylene	400 °C	0.01 ppm	170 (10 ppm)	[101]
Au-$CuFe_2O_4$	Nanoparticles	Xylene	260 °C	/	38.1 (100 ppm)	[108]
Ru-WO_3	Nanosheets	Xylene	280 °C	25 ppb	73 (100 ppm)	[107]

ness of the electron depletion layer, which may suppress the recombination of separated electron hole pairs and cause significant changes in resistance when exposed to the target gas, resulting in higher response. On the other hand, there is the chemical sensitization effect, where precious metals can promote the dissociation of oxygen molecules, producing more reactive chemisorbed oxygen ions, which then overflow onto the SMO surface and react with more target gas molecules [96–99].

Recently, many studies have confirmed in the field of gas senor, the semiconductive nanocomposites supported by noble metals have better sensing sensitivity (Table 3) [91,99,100,89,101–108].

Ag is extensively used to modify the SMO [109–111]. Davida *et al.* [100] reported a Ag/Bi_2O_3 nanocomposite-based gas sensor that has high sensitivity towards toluene gas at room temperature. The experimental result shows that the Ag/Bi_2O_3-based sensors have response of 89.2 % while the pure Bi_2O_3-based sensors have just 15.7 %, as performed in Figs. 5a and b.

Ruthenium (Ru) is another noble metal that acts as a catalyst. Wang *et al.* [107] loaded Ru metals onto the typical sensing material WO_3 [112–114] and improved the selectivity and sensitivity of pure WO_3. The SEM image of the Ru-decorated WO_3 nanosheet is shown in Fig. 5c. According to the gas sensing test shown in Fig. 5d, 0.5 wt% Ru-WO_3-based sensor exhibits the highest response when exposed to 100 ppm xylene, and the limit of detection is 25 ppb. It can be confirmed from Fig. 5e that, compared with Au, Pt and Pd-loaded WO_3 gas sensors, the Ru-loaded WO_3 sensor shows the best sensing property to xylene detection. There are three main reasons to explain the sensing result. Firstly, the number of active sites are increased. The addition of Ru decreased the content of lattice oxygen (O_L) and increased the content of oxygen vacancies (O_V) and chemisorbed oxygen (O_C). Secondly, Ru acts as a catalyst for the decomposition reaction of the targeted gas (xylene). Thirdly, there is a p-n heterojunction between WO_3 and RuO_2 which can change the electrical conductivity.

Besides, noble metal modification for sensing materials can also enhance their selectivity because of the specific reactions that occur between a specific precious metal and a specific gas [98]. Therefore, Kim *et al.* [99] displayed two kinds of sensing materials of ZnO NWs which were functionalized with Pt and Pd respectively. The Pt-functionalized ZnO NWs are prepared by a magnetron sputtering method and show great selectivity to toluene, while the Pb-functionalized ZnO NWs are prepared by an ultraviolet (UV) irradiation reduction technique and are sensitive to xylene (Figs. 5f and h). The reason why these two sensing materials have different selectivity is that Pt and Pd have unique catalysis toward toluene and benzene, respectively. The sensing test result shown in Figs. 5g and i also demonstrated the addition of Pt and Pd improved the sensitivity of the sensor. At room temperature, the sensor made of Pd-functionalized ZnO NWs shows response value of 2.20–50 ppm benzene, and the sensor made of Pt-functionalized ZnO NWs have response of 2.86–50 ppm toluene.

Nowadays, there are many achievements in using noble metal to modify sensing materials, and the addition of noble metal can work out the weakness of the single metal oxide sensing material. However, noble metals with nanostructure also have a series of shortages, for example, it is easy to be oxidized in air and agglomerate at higher operating temperatures. So, whether the properties of the composites can be stable under the high working temperature is still a problem to solve. What's more, the reserves of precious metals are small and expensive. With the development of single atom-catalyst and double atoms-catalyst, loading precious metal components in the form of atoms on the surface of MOS can maximize the catalytic effect with the smallest amounts of precious metals, which is beneficial for commercial development [95,99,89,104].

3.2. Heterojunction between double MOSs

Usually, composite materials formed between different types of MOS also exhibit exciting gas sensing performance (Table 4) [115–117,41,118–137]. This is mainly attributed to the transfer of electrons and holes at the interface between different MOS components, until their Fermi levels balance to the same level, thus forming a heterojunction between MOS [41,119,120,122]. The formation of heterojunctions can change the electron distribution between different MOS components, adjust the thickness and barrier height of the electron depletion layer, and thus achieve the goal of changing the sensing performance of gas sensitive materials. The heterojunctions formed between MOS mainly include hetero-type junctions (p-n/n-p junctions) and isotype junctions (n-n/p-p junctions) [123,124,128,132].

For isomorphic heterojunctions (p-n type, n-p type), when the two MOSs with different Fermi levels come into contact with each other, electrons transfer from the n-type MOS with higher Fermi levels to the p-type MOS with lower Fermi levels. The direction of hole transfer is opposite until the two Fermi levels are in equilibrium and a depletion layer is formed at their interface. The energy bands on both sides bend to form a potential barrier, making the electron transfer channel a near propeller flow. In addition, due to the wide depletion layer width of heterojunctions, the initial resistance of composite materials is much greater than that of MOS. Therefore, when exposed to reducing gases such as BTX, the resistance of the composite gas sensitive material sharply decreases, improving the sensitivity and selectivity of the sensing materials. The BTX gas sensing mechanism of the MOS isomorphic heterojunction is shown in Fig. 6a. For instance, SnO_2–NiO foam was a n-p type heterostructure, created by a dip-coating method [122]. The Field Emission Scanning Electron Microscope (FESEM) image

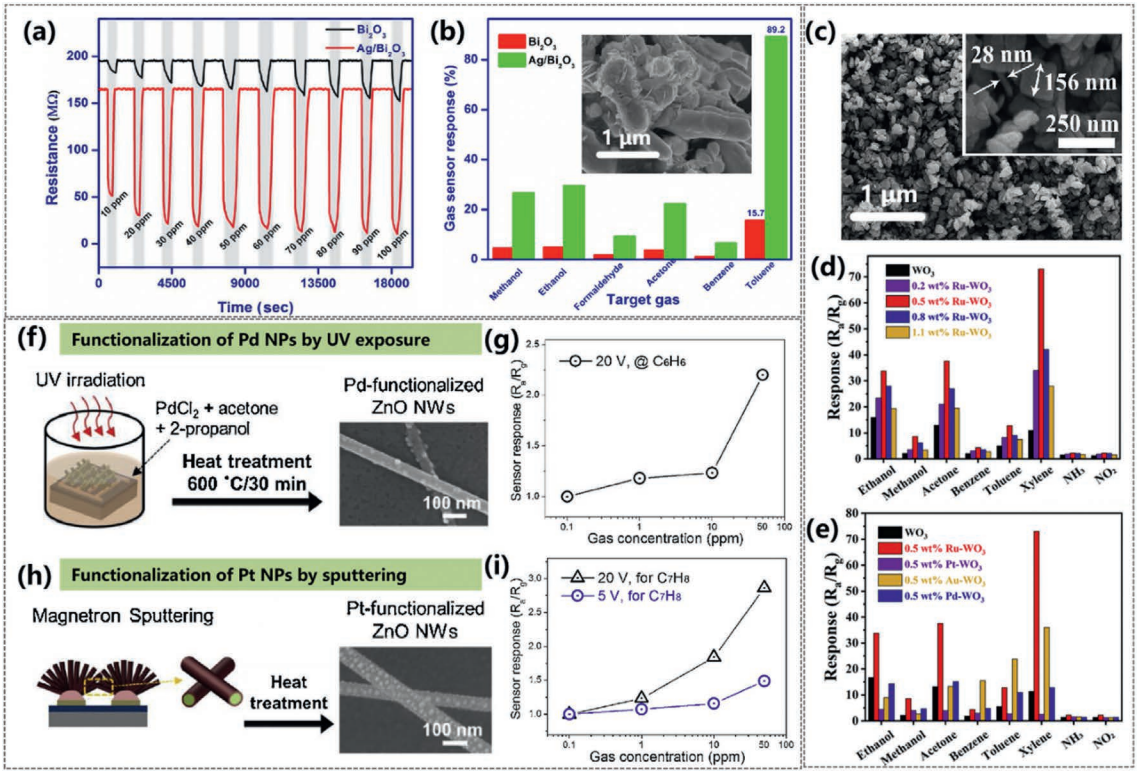


Fig. 5. (a) Resistance of the gas sensor being alternatively exposed to air and toluene gas for both Bi_2O_3 and Ag/Bi_2O_3 at 10–100 ppm. (b) Gas sensor response of Bi_2O_3 and Ag/Bi_2O_3 against 50 ppm concentration of six different gases formaldehyde, acetone, methanol, ethanol, benzene and toluene at room temperature. (a, b) Reprinted with permission [100]. Copyright 2020, Elsevier. (c) SEM images of 0.5 wt% Ru-WO_3. (d) The sensor response to 100 ppm ethanol, methanol, acetone, benzene, toluene, xylene, NH_3 and 1 ppm NO_2. (e) The response of sensors based on 0.5 wt% Ru, Pt, Pd and Au loaded WO_3 to 100 ppm ethanol, methanol, acetone, benzene, toluene, xylene, NH_3, and 1 ppm NO_2. (c-e) Reprinted with permission [107]. Copyright 2020, Elsevier. (f) Illustration of Pd NPs synthesis procedure. (g) The corresponding response of Pd-ZnO NWs *versus* benzene concentration. (h) Illustration of Pt NPs synthesis procedure. (i) Responses of Pt-functionalized ZnO NWs derived from 5 nm Pt layer deposited on ZnO NWs to various concentrations (0.1–50 ppm) of toluene (C_7H_8) at 20 V and 5 V. (f-i) Reprinted with permission [99]. Copyright 2019, Elsevier.

and Optical Microscope (OM) image are shown in Figs. 6b and c. The SnO_2–NiO foam n-p type heterojunction shows the response of 19.2 at 10 ppm toluene under optimum conditions significantly surpassing that of the p type MOS pure NiO (Fig. 6d). Notably, the gas response and recovery time were only 9 s and 8 s, respectively, and consistent operation was demonstrated for at least 30 days. Not come singly but in pairs, Guo *et al.* [129] fabricated hierarchical p-n type CuO-WO_3 heterojunction using ultrasonic-wet chemical etching and pyrolysis. The structure of core-shell microspheres, assembled from irregular 2D nanosheets and the synthesis method are shown in Figs. 6e and f. CuO-WO_3 gas sensing materials exhibited enhanced gas-sensing capabilities in response and response/recovery time compared to pristine WO_3 n type materials which is shown in Figs. 6g and h. Furthermore, CuO/WO_3 sensing materials demonstrated long-term stability, attributed to their CuO-WO_3 p-n heterojunction and distinctive 3D hierarchical structure, which has also been confirmed in Wang's research [117]. In Hermawan's research [121], SnO_2–CuO n-p heterojunctions with CuO NPs and spherical SnO_2, with a high specific surface area (exceeding 90 m^2/g) were successfully synthesized using a non-hydrolytic approach. The p-n heterojunction structure, combined with the high specific surface area and porous properties, resulted in the sensing response of SnO_2–CuO to toluene gas ($R_a/R_g = 540$ at 75 ppm), accompanied by outstanding gas selectivity. Also, exposure to high concentrations of toluene caused the formation of Cu metal, disrupting the p-n junction and creating an ohmic contact with the n-type material, further enhancing the gas sensing properties.

For homogeneous heterojunctions (n-n type, p-p type), the phenomenon of band bending and potential barrier formation can also occur due to changes in the Fermi level. For n-n heterojunctions, electrons transfer from the high Fermi level side to the low Fermi level side, with an electron depletion layer formed on the high Fermi level side and an electron accumulation layer formed on the other side. However, for p-p heterojunctions, holes transfer from the low Fermi level side to the high Fermi level side, with a hole accumulation layer formed on one side of the high Fermi level and a hole depletion layer formed on the other side [120,121]. Exposure to BTX will help consume surface oxygen and inject electrons into the surface to reduce the depletion layer (Fig. 7a). Formed a significant reduction in resistance and achieved higher gas sensing performance. Qu *et al.* [130] synthesized hierarchical p-p type Co_3O_4–$NiMoO_4$ core-shell nanowires (CSNWs) through a two-step hydrothermal process. The SEM and TEM images of the Co_3O_4–$NiMoO_4$ CSNWs are shown in Figs. 7b and c. These NWs exhibit a response of 24.6 (R_{gas}/R_{air}) in 100 ppm xylene at 255 °C which is nearly 2 times larger than the response of pure Co_3O_4 NWs. Moreover, the p-p type Co_3O_4–$NiMoO_4$ heterojunction shows great selectivity of xylene compared to toluene, benzene, ethanol, acetone, *etc.* (Fig. 7d). These exceptional gas-sensing properties result from the synergistic catalytic effects and the Co_3O_4–$NiMoO_4$ heterostructure. Another range of p-p heterojunctions with different $NiGa_2O_4$–NiO composites has been systematically fabricated by Chen *et al.* [123] through a straightforward solvothermal method (Fig. 7e). The $NiGa_2O_4$–NiO p-p type heterostructure consisting of 50 wt% $NiGa_2O_4$ has demonstrated superior sensing capabilities, showing a substantial response ($R_g/R_a = 12.7$–100 ppm of toluene; $R_g/R_a = 16.3$–100 ppm of xylene) as shown in Figs. 7f and g. The enhanced sensing attributes are primarily attributed to the optimized p-p heterojunction structure, which facilitates the transfer

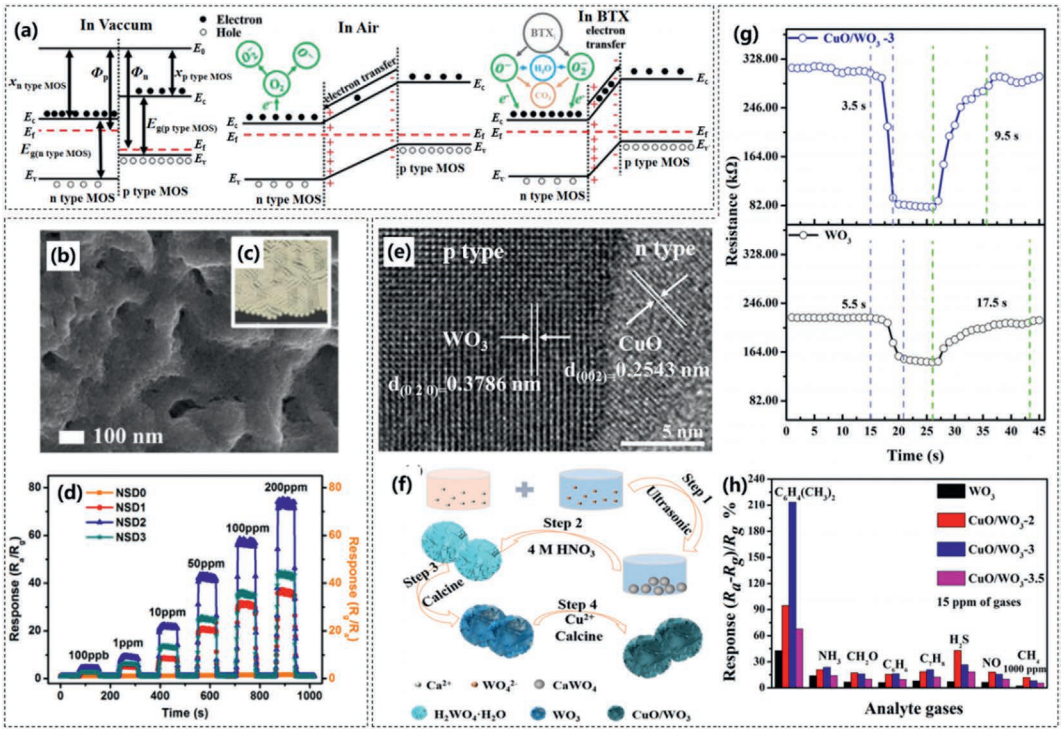


Fig. 6. (a) Energy band structure of the MOS isomorphic heterojunction in vacuum, contact situation in air and BTX environment. (b, c) FESEM and OM images of NSD2. The SnO_2-decorated NiO foam with dip-coating 2 times. (d) Dynamic response curves of SnO_2-decorated NiO foam with different dip-coating time in 0.1–200 ppm toluene at 205 °C. (a-d) Reprinted with permission [122]. Copyright 2020, Elsevier. (e) HRTEM images of CuO/WO_3–3. (f) Synthetic scheme of WO_3 and CuO/WO_3 hierarchical structure. (g) The transient responses of WO_3 and CuO/WO_3–3 (The mass ratio of CuO to WO_3 is 3%) gas sensing materials to 20 ppm xylene at 260 °C. (h) The selectivity of WO_3 and different CuO/WO_3 gas sensing materials to 15 ppm xylene gas and other gases. (e-h) Reprinted with permission [129]. Copyright 2020, Elsevier.

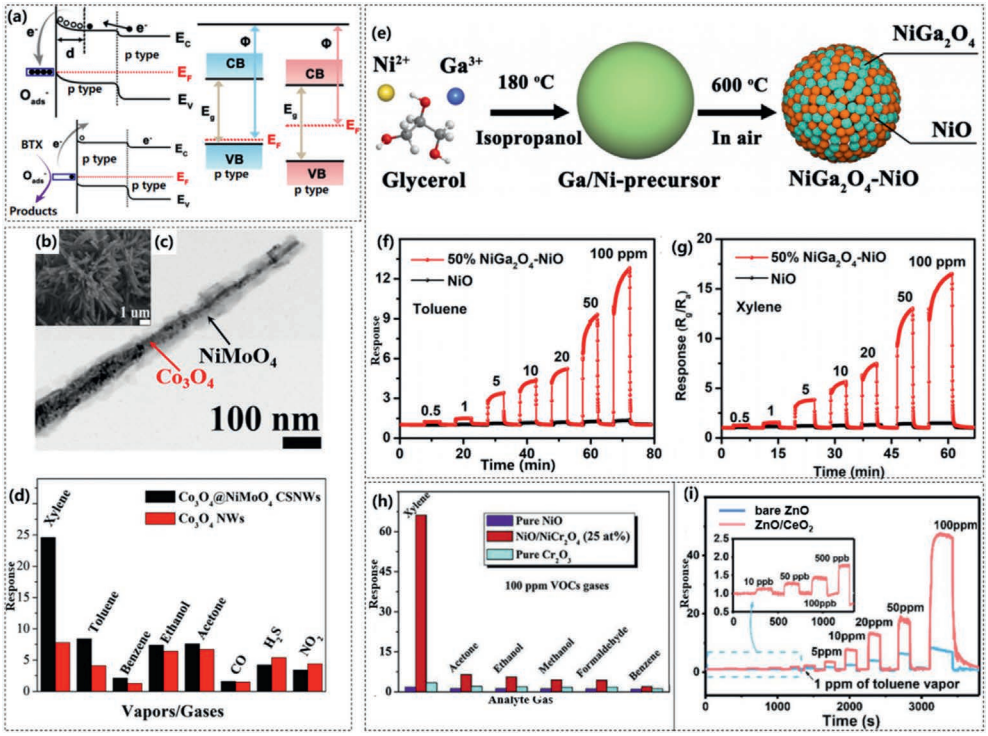


Fig. 7. (a) Energy band structure of the MOS homogeneous heterojunction in vacuum, contact situation in air and BTX environment. (b, c) SEM and TEM images of Co_3O_4–$NiMoO_4$ CSNWs. (d) Cross-responses of Co_3O_4 NWs and Co_3O_4–$NiMoO_4$ CSNWs to various gases at 255 °C. (a-d) Reprinted with permission [128]. Copyright 2019, Springer Nature. (e) Schematic illustration of the synthesis of $NiGa_2O_4$–NiO sample. (f, g) Dynamic sensing transients of 50% $NiGa_2O_4$–NiO and pristine NiO toward toluene and xylene in the concentration range of 0.5–100 ppm at 230 °C. (e-g) Reprinted with permission [123]. Copyright 2019, Elsevier. (h) Selectivity of the NiO, NiO/$NiCr_2O_4$ (Cr/Ni = 25 at%) and Cr_2O_3 samples. Reprinted with permission [132]. Copyright 2019, Elsevier. (i) Response curves of the ZnO–CeO_2 and bare ZnO for toluene vapors with concentrations in the range of 10 ppb to 100 ppm. Reprinted with permission [117]. Copyright 2020, Royal Society of Chemistry.

Table 4
BTX gas sensing materials - Heterojunctions between double MOSs.

Material	Morphology	Sensitive gas	Optimal working temperature	Limit of detection	Response (concentration)	Refs.
$0.5SnO_2$–$0.5Co_3O_4$	Nanofibers	Benzene	350 °C	/	18.7 (1 ppm)	[115]
ZnO–CdO	Nanoflakes	Benzene	Room temperature	1 ppm	453 (100 ppm)	[116]
ZnO–CeO_2	Porous and layer	Benzene	20 °C	/	10.3 (50 ppm)	[117]
SnO_2–NiO	Nanoparticles	Toluene	250 °C	1.2 ppb	60 (100 ppm)	[41]
Co_3O_4-WO_3	Hollow spheres	Toluene	225 °C	1 ppm	55.8 (100 ppm)	[118]
$Fe_xNi_{(1-x)}O$–NiO	Hybrid heterostructures	Toluene	250 °C	0.83 ppm	1.5 (76 ppm)	[119]
NiO-ZnO	Hollow microspheres	Toluene	300 °C	100 ppb	240 (100 ppm)	[120]
SnO_2–CuO	Nanoparticles	Toluene	400 °C	/	540 (75 ppm)	[121]
SnO_2–NiO	Nanospheres	Toluene	205 °C	/	19.2 (10 ppm)	[122]
$NiGa_2O_4$–NiO	Spherical shapes	Toluene	230 °C	/	12.7 (100 ppm)	[123]
$NiGa_2O_4$–NiO	Layer sheets	Toluene	200 °C	/	10.48 (5 ppm)	[124]
In_2O_3-ZnO	Nanofibers	Toluene	Room temperature	1 ppm	14.6 (100 ppm)	[125]
$Cr_2O_3/ZnCr_2O_4$	Nanoparticles	Xylene	275 °C	/	69.2 (5 ppm)	[126]
SnO_2–Co_3O_4	Nanoparticles	Xylene	175 °C	0.05 ppm	101.9 (100 ppm)	[127]
Co_3O_4–$NiMoO_4$	Core-shell nanowires	Xylene	255 °C	424 ppb	24.6 (100 ppm)	[128]
CuO-WO_3	2D nanosheets	Xylene	260 °C	/	6.36 (50 ppm)	[129]
Fe_2O_3–MoO_3	Nanobelts	Xylene	233.5 °C	/	22.48 (100 ppm)	[130]
NiO–$NiCo_2O_4$	Nanorods	Xylene	Room temperature	0.5 ppm	4 (50 ppm)	[131]
NiO–$NiCr_2O_4$	Nanoparticles	Xylene	225 °C	0.05 ppm	66.2 (100 ppm)	[132]
SnO_2–Co_3O_4	Nanorods	Xylene	280 °C	/	47.8 (100 ppm)	[133]
Co_3O_4-In_2O_3	Nanoplates	Xylene	150 °C	0.2 ppm	36.6 (100 ppm)	[134]
$NiTiO_3$–NiO	Nanosheets	Xylene	387 °C	1 ppm	21 (100 ppm)	[135]
CuO-ZnO	Nanorods	Xylene	100 °C	9.5 ppb	10.9 (100 ppm)	[136]
WO_3–NiO	Hollow microspheres	Xylene	300 °C	1.5 ppb	354.7 (50 ppm)	[137]

of electrons from $NiGa_2O_4$ to NiO, enhances oxygen adsorption on the NiO surface, thereby augmenting the catalytic effect of NiO in oxidizing toluene and xylene. In Gao's research [132], another Ni based p-p type heterojunction NiO–$NiCr_2O_4$ was synthesized with a Cr/Ni ratio of 25 at%. The p-p type heterojunction NiO–$NiCr_2O_4$ comprised a homogeneous blend of small NiO and $NiCr_2O_4$ NPs and demonstrated robust xylene response 66.2 at 100 ppm (Fig. 7h) and an impressively low LOD at 50 ppb. Furthermore, the p-p type heterojunction NiO–$NiCr_2O_4$ exhibited exceptional xylene sensitivity.The outstanding capability for xylene detection can be attributed to the formation of the nanoscale p-p NiO–$NiCr_2O_4$ heterojunctions, large surface area and the synergistic catalytic promotion of NiO and $NiCr_2O_4$ NPs. Additionally, the n-n type heterojunction has been synthesized in Wang's research [117], which revealed that the triangular CeO_2 nanoflake enhanced the response of ZnO-based gas sensing materials to BTX vapors. The response values (R_a/R_g) of the n-n type ZnO–CeO_2 heterojunction gas sensing material to 50 ppm benzene, toluene and xylene were 10.3, 20.3 and 19.7 respectively which is more than three times higher and a quicker response than the n type bare ZnO (Fig. 7i). Notably, the n-n type ZnO–CeO_2 heterojunction bi-layer sensor detected toluene vapor at under 10 ppb. In conclusion, the homogeneous heterojunctions (n-n, p-p) and the isomorphic heterojunctions (p-n type, n-p type) of MOS can both increase the response, selectivity and response/recovery time in detecting BTX gas molecules, which can significantly attribute to the charge distribution, depletion/barrier layers formation and the balance of the different Fermi levels at the interface of the two MOSs.

3.3. Other heterojunction

To achieve high gas sensitivity, MOS-based sensing material often requires operation at high temperatures, resulting in significant energy consumption [138]. And some porous structures are prone to structural alterations and exhibit reduced stability at elevated temperatures, thereby posing challenges for sustained long-term operation. Furthermore, with the development of wearable electronic device, flexible gas sensors also obtain human's attention which can not work at a high temperature. Therefore, the research on metal oxide semiconductors for low-temperature or room temperature detection is also very meaningful. The current common method to reduce the working temperature of MOS-based BTX sensing materials is to form composite materials by combining MOS with carbon-based materials, conductive polymers, and other substances. The summary of the published work is shown in Table 5 [139–152].

Several researches have revealed that carbon-based materials, such as graphene, carbon nanotubes, carbon dots and so on, possess a degree of gas adsorption affinity in ambient environments with their ensuing electrical properties post-gas adsorption being contingent upon the specific type of gas adsorbed [153–156]. This discovery establishes a fundamental framework for the utilization of carbon-based materials in gas detection. In the course of this part of study, researchers have orchestrated the integration of carbon-based materials with metal oxides, thereby fostering a mutually reinforcing synergy between the two components, effectively harnessing their complementary attributes. Guo *et al.* [142] present a new single-step hydrothermal method for synthesizing bismuth (Bi)-doped SnO_2/reduced graphene oxide (rGO) nanocomposites for enhanced gas sensing applications. The gas sensing properties of the resulting Bi-doped SnO_2/rGO composite were extensively improved compared to pure SnO_2 and rGO/SnO_2 counterparts, particularly for benzene detection (Fig. 8a). Notably, the Bi-doped SnO_2/rGO nanocomposite exhibited remarkable enhancements in gas response, rapid response-recovery kinetics, sustained stability, and excellent selectivity, positioning it as a prime candidate for benzene detection (Fig. 8b). The superior gas sensing characteristics of the Bi-doped SnO_2/rGO nanocomposite were attributed to its augmented specific surface area resulting from the unique composite structure, the distinctive rGO-SnO_2 heterojunctions, the narrowed band gap, and the abundance of oxygen vacancies. Onthath's study [157] linked to carbon-based material introduces a nanocomposite of copper oxide (CuO) NPs and carbon nanotubes (CNTs) for effective BTX detection. Furthermore, the sensor detects benzene even at concentrations as low as 5 ppm. Given its high sensitivity, the CNT/CuO nanocomposite is suitable for detecting benzene even at low concentration levels. In addition, some works used porphyrin and its derivatives to functionalize metal oxide semiconductors, which is widely used in fields such as electrocatalysis and is rare in the field of gas sensing. Kang *et al.* [158] proposed a sen-

Table 5
BTX gas sensing materials - Other types of heterojunctions.

Material	Morphology	Sensitive gas	Optimal working temperature	Limit of detection	Response (concentration)	Refs.
CNT-CuO	Nanoparticles	Benzene	Room temperature	5 ppm	0.62 (500 ppm)	[139]
Graphene-SnO_2/WO_3	Nanoparticles	Benzene	250 °C	200 ppb	1.0 (2 ppm)	[140]
GaN-TiO_2	Nanowire	Benzene	Room temperature	50 ppb	1.50 (1000 ppm)	[141]
Bi-doped SnO_2-rGO	Spheres	Benzene	150 °C	0.3 ppm	48.6 (5 ppm)	[142]
PANI–SnO_2	Nanoscale particles	Benzene	Room temperature	0.4 ppm	1.01 (20 ppm)	[143]
ZnO-BNQD	Nanoplates	Benzene	300 °C	/	2.07 (100 ppm)	[144]
CuO-$Ti_3C_2T_x$	Nanospheres	Toluene	250 °C	/	11.4 (50 ppm)	[145]
V_2O_5-GO	Nanohybrid	Toluene	Room temperature	5 ppm	32.65 (60 ppm)	[146]
CdS-SnO_2	Nanofilms	Toluene	200 °C	/	51 (5000 ppm)	[147]
Ni/Fe MOF-$NiFe_2O_4$	Nanorods	Toluene	200 °C	1 ppm	60 (500 ppm)	[148]
Co-doped C_3N_4-ZnO	Porous sheets	Xylene	370 °C	/	32.6 (100 ppm)	[149]
Ni$(OH)_2$–Co_3O_4	Nanoplates	Xylene	175 °C	100 ppb	14.1 (100 ppm)	[150]
SnO_2—MWCNTs	Nanoparticles	Xylene	220 °C	/	0.15 (3.6 ppm)	[151]
rGO–Co_3O_4	Nanoparticles	Xylene	175 °C	1 ppb	8.31 (50 ppm)	[152]

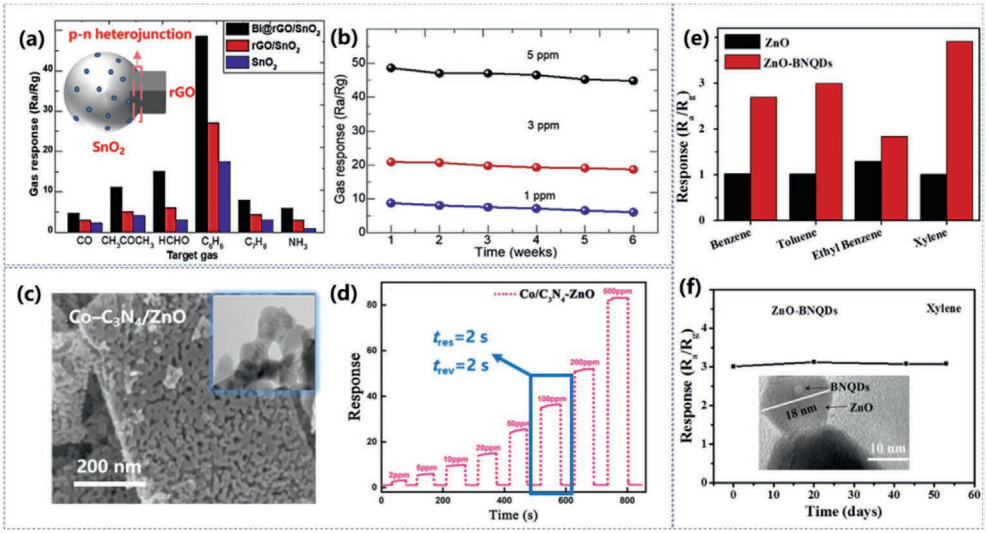


Fig. 8. (a) The gas responses of sensors based on SnO_2, rGO/SnO_2 and Bi@rGO/SnO_2 to 5 ppm various typical indoor harmful volatile gases. (b) The long-term gas response stability of the sensor based on Bi@rGO/SnO_2 at different conditions (1, 3, and 5 ppm benzene) for 6 weeks intervals at 150 °C in 30 % RH. Reprinted with permission [142]. (a, b) Copyright 2019, Elsevier. (c) SEM images of Co–C_3N_4/ZnO. (d) Responses of Co–C_3N_4/ZnO sensor against different concentrations of p-xylene at 370 °C. (c, d) Reprinted with permission [149]. Copyright 2020, Springer Nature. (e) Responses of pure ZnO nanoplates and ZnO-BNQDs sensors to 100 ppm BTEX at 370 °C. (f) Response stability of ZnO-BNQDs sensor to 100 ppm xylene at 370 °C conducted for a period of more than 50 days. (e, f) Reprinted with permission [144]. Copyright 2020, Elsevier.

sor using cobalt porphyrin (CoPP)-functionalized TiO_2 nanoparticles on a suspended microheater. This design improves sensitivity, achieving a 245 % enhancement for 10 ppm toluene detection, and demonstrates reliable detection of BTX from 10 ppm to several ppb, with stable performance over 14 h of repeated exposure.

Development of wearable and flexible gas sensors has been a prominent research focus in the field of gas sensors currently [25,159–163]. Conductive polymers, due to their excellent flexibility and distinct changes in resistance in various gas environments, have been regarded as promising materials for flexible gas sensors [164–166]. An interesting research studied by Feng *et al.* [143] involves synthesizing polyaniline (PANI) *via* chemical oxidative polymerization of aniline under acidic conditions, followed by doping with tin dioxide (SnO_2) at a specific ratio. The resulting PANI/SnO_2 hybrid material is ground at room temperature, forming nanoscale particles with favorable dispersibility for gas adsorption. Gas sensing tests are conducted at 20 °C and 40 % ± 5 % relative humidity, examining concentrations of 0.4–90 ppm for benzene vapor in both PANI and PANI/SnO_2 hybrid materials. PANI/SnO_2 hybrid material boasts shorter recovery times and a broader detection range than PANI alone, underscoring its enhanced capabilities.

In addition, there are studies that utilize the combination of metal oxides with other semiconductors to form gas-sensitive materials, such as the composite with nitrides and nitride quantum dots. Hu *et al.* [149] successfully prepared a Co-doped g-C_3N_4 and ZnO nano-composite (Co–doped C_3N_4/ZnO) sensing materials using a solid-phase precursor synthesis method (Fig. 8c). The gas sensing performance of the Co–doped C_3N_4/ZnO sensor was systematically studied and compared with other sensors at temperatures ranging from 200 °C to 370 °C, with the highest response observed at 370 °C. Remarkably, the Co–doped C_3N_4/ZnO sensor exhibited an 11-fold higher response compared to the pure ZnO sensor at 370 °C for xylene detection. Additionally, the sensor demonstrated excellent stability and repeatability even after 14 weeks, with a rapid response/recovery time of 2 s/2 s (Fig. 8d). The enhanced gas sensing performance was attributed to the presence of more active sites and a higher number of active oxygen species on the ZnO surface. The composite of porous ZnO nanosheets and Co-doped C_3N_4, prepared through solid-phase synthesis, exhibits remarkable gas sensing ability. A gas sensor using boron nitride quantum dots (BNQDs) on ZnO nanoplates was developed for BTX vapors, synthesized by a solvothermal mean [144], with the distinct ZnO-BNQDs heterojunction. Particularly, the ZnO-BNQDs showed superior BTX detection, especially xylene, over 3.5 times more sensitive than pure ZnO and the response over 50 days was still stable (Figs. 8e and f). BNQDs on ZnO introduced active sites, boosting catalytic oxidation of BTX. ZnO-BNQDs responded better at varied temperatures due to BNQDs sensitization.

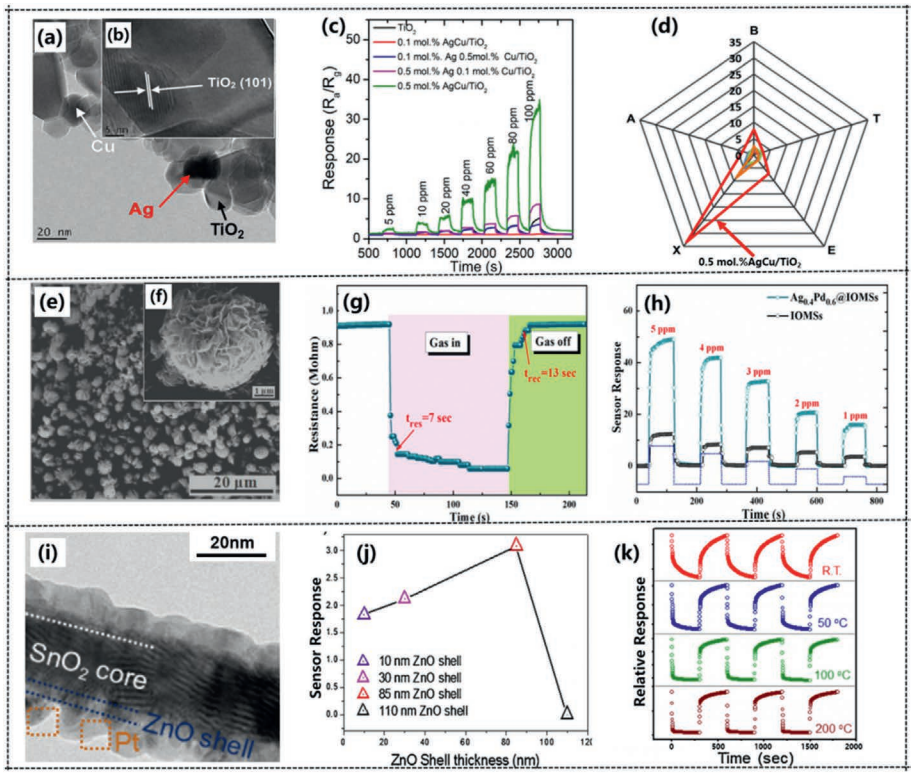


Fig. 9. (a, b) The TEM images of Ag-Cu/TiO_2 NPs. (c) The real-time response curve of the Ag-Cu/TiO_2 towards xylene. (d) Radar selectivity plot. Letter A corresponds to acetone, while the others are BTEX in a radar plot. (a-d) Reprinted with permission [167]. Copyright 2022, Royal Society of Chemistry. (e, f) FESEM images of $Ag_{0.4}Pd_{0.6}$–In_2O_3. Reprinted with permission [132]. Copyright 2022, Elsevier. (g) Dynamic response and recovery time curve of $Ag_{0.4}Pd_{0.6}$–In_2O_3. (h) The representative dynamic sensing curves of $Ag_{0.4}Pd_{0.6}$@In_2O_3 and pristine In_2O_3 to toluene in the low concentration range (1–5 ppm) at 180 °C. (g, h) Reprinted with permission [168]. Copyright 2022, Elsevier. (i) Low magnification TEM micrograph of a Pt NP-functionalized SnO_2–ZnO CSNWs. (j) Variation of response to toluene gas with varying the thickness of ZnO shell layer. (k) Dynamic resistance curves of Pt-functionalized SnO_2–ZnO CSNWs with a ZnO shell thickness 85 nm. (i-k) Reprinted with permission [170]. Copyright 2017, Elsevier.

4. BTX gas sensing materials comprising three or more substances

For single component and single heterojunction gas sensitive materials of metal oxide semiconductors, only a certain aspect of the gas sensitive material's performance can be significantly changed through heterostructure. There is still room for improvement in sensitivity, selectivity, and operating temperature for target gas detection [167–171]. Therefore, researchers have employed multi-component composites composed of three or more substances, aiming to fabricate gas-sensitive materials with enhanced sensitivity [172–174], improved selectivity [175–177], and lower working temperature [32,178].

A common material design strategy is to first composite metal oxide semiconductors with other substances to form one of the heterostructures, which can adjust morphology, achieve surface reactions, and change space charge distribution, thereby improving gas sensing sensitivity. Then, noble metals are loaded on the surface to form another heterostructure, which catalyzes surface chemical reactions, reduces activation energy, and achieves low-temperature detection. Maake *et al.* [167] synthesized the timely and selective material n-type Ag-Cu/TiO_2 NPs for detecting xylene vapor in various vapors at low temperatures (Figs. 9a and b). Notably, the sensor's switching behavior between p-type and n-type conductivity remains independent of temperature or the specific gas detected. The n-type 0.5 % Ag-Cu loaded on TiO_2 exhibits a remarkable response ($R_g/R_a = 33.2$) to xylene vapor at 150 °C, with superior selectivity compared to individual Cu or Ag loading on a TiO_2 sensor (Figs. 9c and d). The improved xylene gas sensing is attributed to the catalytic activity and point defects induced by Ag-Cu loading in TiO_2, driven by the strong synergistic catalytic influence of the n-type Ag-Cu/TiO_2 NPs, reducing activation energy and accelerating xylene reaction with oxygen species. In another study, sensitive materials based on Ag/Pd–In_2O_3 were synthesized by Liu *et al.* using a hydrothermal method and subsequent *in situ* reduction treatment for investigating their toluene sensing performance [168]. The FESEM images are shown in Figs. 9e and f. The $Ag_{0.4}Pd_{0.6}$–In_2O_3 gas sensing materials demonstrated high response towards 1 ppm toluene gas at a low operating temperature of 180 °C, with remarkably short response and recovery times of 7 and 13 s, respectively, along with a low detection limit of 20 ppb (Figs. 9g and h). These exceptional gas sensing attributes were attributed to the unique structures of the materials, the electronic sensitization effect of Ag/Pd NPs, and the presence of abundant oxygen vacancies at the surface. Kim *et al.* [170] successfully developed Pt–SnO_2–ZnO CSNWs toluene gas sensing materials (Fig. 9i). Both Pt NPs and the ZnO shell contributed to the enhanced sensing of C_7H_8 gas. The response increased with thicker ZnO shell thickness in the tested range of 10–85 nm (Fig. 9j). The dominant role of ZnO-ZnO homojunctions in achieving self-heating effects was concluded from the analysis of possible self-heating mechanisms of the ZnO shell. Furthermore, the responses amplified with gas concentrations within the ranges of 100 ppb-50 ppm at room temperature respectively (Fig. 9k) which was attributed to variations in conduction volume, electrical contact between CSNWs, and the effects of Pt catalysts.

This article comprehensively summarizes the current design of multi-component sensing materials composed of three or more substances, as shown in Table 6 [167–174,179–185]. It can be seen that by designing gas sensing materials with multiple heterostruc-

Table 6
BTX gas sensing materials consisting of three or more components.

Material	Morphology	Sensitive gas	Optimal working temperature	Limit of detection	Response (concentration)	Refs.
Pd-rGO-ZnO	Nanofibers	Benzene	400 °C	/	22.8 (50 ppm)	[174]
SnO_2-ZnO-Pd	Random alignment	Benzene	200 °C	/	2.62 (50 ppm)	[179]
Au-SiO_2-SnO_2	Silica particles	Benzene	300 °C	/	8.2 (100 ppm)	[180]
Si–TeO_2–Pd	Nanoparticles	Benzene	200 °C	/	55.19 (50 ppm)	[181]
Pd-Bi_2O_3–ZnO	Nanorods	Benzene	300 °C	/	28.0 (200 ppm)	[182]
Pt-SnO_2–ZnO	Nanowires	Benzene	Room temperature	0.5 ppm	3.14 (50 ppm)	[170]
Ag-Pd-In_2O_3	Flower-shaped	Toluene	180 °C	20 ppb	15.9 (1 ppm)	[168]
Au-NiO-In_2O_3	Hollow microspheres	Toluene	250 °C	5.1 ppb	80.6 (10 ppm)	[169]
Au-Pd-Co_3O_4-ZnO/ZnO	Nanoparticles	Toluene	250 °C	100 ppb	256 (100 ppm)	[183]
Pt-MoO_3-mpgCN	Mesoporous channels	Toluene	175 °C	/	34.1 (25 ppm)	[173]
Pd-PdO-SnO_2	Nanofibers	Toluene	285 °C	50 ppb	132 (100 ppm)	[184]
Si-TeO_2-Pt	Nanowires	Toluene	200 °C	/	45 (50 ppm)	[185]
Ag-Cu-TiO_2	Nanoparticles	Xylene	150 °C	0.03 ppm	33.2 (100 ppm)	[167]
(Fe_2O_3+TiO_2+MgO)/(WO_3+TiO_2)-Ni	Cylindrical	Xylene	340 °C	0.07 ppm	4.2 (1 ppm)	[172]
Au-Pd-SnS_2	Hexagonal	Xylene	161 °C	10 ppm	27.7 (100 ppm)	[171]

tures, a very low detection limit can be achieved. For example, Sun *et al.* [169] presents a sensor based on Au nanoparticle modified MOF derived NiO/In_2O_3 hollow microspheres, which demonstrate high sensitivity and fast response/coverage to lecture, with a detection limit of 5.1 ppb. Such high-performance materials have great application prospects in the detection and monitoring of ppb level BTX in atmospheric environments.

5. Conclusions and future perspectives

Compared to other expensive gas detection equipment, chemiresistive gas sensors have shown great potential in monitoring BTX gases, making the study of these sensors highly significant. In this review, we systematically analyze the research progress on chemiresistive gas sensors for BTX gas concentration detection [186–190]. Since the performance of gas-sensitive materials directly determines the sensitivity, selectivity, and subsequent application scope of the gas sensor, this paper focuses on the current research on gas-sensitive materials. Based on the composition of the sensitive materials, we categorize them into three types: gas sensors with single-component gas-sensitive materials, those with one heterojunction gas-sensitive materials, and those with multiple heterojunctions gas-sensitive materials. Furthermore, we discuss their fabrication techniques, gas sensitivity, and the advantages and disadvantages of each. In current research, enhancing the performance of gas sensors for BTX gas detection mainly involves improving their sensitivity to the target gas and increasing the selectivity for specific gas detection. The main strategies include designing nanostructures with different morphologies to increase the specific surface area and gas adsorption efficiency, and from a mechanistic perspective, preparing composite materials of various substances to enhance sensitivity and selectivity through the formation of heterogeneous structures or electron sensitization effects. The main conclusions are summarized as follows:

(1) For single component gas sensitive materials, high-performance sensing materials are mainly obtained by changing the morphology and structure of the materials. According to the gas sensing mechanism, the response of gas sensitive materials to gas is related to both the number of adsorption sites and the ratio of electron depletion layer to material core. Therefore, when designing gas sensitive materials, the gas sensing performance can be improved by increasing the specific surface area and reducing the size of the gas sensitive material. For example, hollow structures [191], core-shell structures [192,193], porous mesoporous materials [194,195], and some low dimensional structures such as nanoparticles, one-dimensional nanorods, nanowires, and two-dimensional nanosheets are used [51,196].

(2) Noble metal decoration is one of the most common ways to improve sensing characterization of the sensing materials. The remarkable improvement of gas sensing performance after noble metal decoration could be attributed to two main mechanisms, the electronic sensitization and the chemical sensitization. Electronic sensitization process leads to the formation of a Schottky barrier and an increase in the thickness of the electron depletion layer, which could inhibit the recombination of separated electron–hole pairs and cause a significant change of the resistance when exposed to target BTX gases, resulting in a much higher response. During the chemical sensitization process, the noble metals could facilitate the dissociation of oxygen molecules to produce more reactive chemisorbed oxygen ions which then spill over the surface of semiconductor to react with more target gas molecules [31,197]. What is more, different noble metals are specialized in detecting specific gases, thus enhancing the selectivity of the sensing material for target gas [32,198].

(3) Constructing heterostructures is another way to improve the performance of gas sensitive materials. The heterojunction is formed at the contact interface of two different materials, including an isotype heterojunction (*i.e.*, p–n or n–p) and isotype heterojunction (*i.e.*, n–n or p–p), it could change the electronic band structures to achieve high sensing response. In our summary of research on gas sensing materials for BTX gas detection, gas sensing materials with heterostructures mainly include: metal oxides forming heterostructures with metal oxides [120], metal oxides forming heterostructures with carbon-based materials [151,199,200], metal oxides forming heterostructures with conductive polymers [128], and two or more substances forming multiple heterostructures [167,172,179].

(4) Current research suggests that the preparation of the sensing material depends on the design and control of its morphology and composition, including hydrothermal [201], electrospinning [202,203], flame spray pyrolysis [204,205], sputtering technique [206] and other preparation methods [207,208]. These methods usually have the characteristics of simple synthesis process and environmental protection.

In the realm of BTX gas detection, considerable advancements have been realized in the domain of chemical resistive-based gas sensors. However, current commercial semiconductor gas sensors still exhibit limitations, including slow response and recovery speeds, and high operating temperatures [30,31], thus numerous

obstacles persist in the pursuit of critical performance improvement and their practical implementation. This review encapsulates the ensuing challenges and forthcoming opportunities in the development of chemical resistive-based gas sensors tailored for BTX gas detection, which are delineated as follows:

(1) In the current landscape of gas sensor technology, metal oxide-based gas sensors are predominant; however, they typically necessitate higher operating temperatures. In practical application scenarios, such as the detection of BTX gas leaks in chemical plants, these elevated temperatures may pose a risk of igniting fires, consequently limiting their practical utility. Present research on low-temperature or room-temperature gas sensors is not yet mature, exhibiting drawbacks such as poor stability and prolonged response and recovery times. Therefore, further research is imperative in developing chemiresistive gas sensors for BTX gas detection at lower temperatures.
(2) According to the summarized research progress, the detection lower limit of most gas sensitive materials is at the ppm level, and for the human body, long-term inhalation of ppb level BTX gas already poses a risk of leukemia. Therefore, achieving ppb level ultra-low concentration gas detection is still worth further in-depth research.
(3) BTX substances will be further miniaturized and integrated into portable and wearable devices as they can be used as good solvents in common household items such as paints, fuels, and cleaning agents. This will enable individuals to monitor the air quality of their environment in real-time, reducing the incidence of leukemia.
(4) In recent years, chemiresistive gas sensors have undergone substantial development, and the construction of sensor arrays has emerged as a method to enhance the selectivity and accuracy of gas detection. The integration of BTX gas sensors with other gas sensors into an array not only facilitates high sensitivity and selective detection of specific BTX compounds but also enables simultaneous monitoring of other harmful gases. Such integration contributes to the creation of multifunctional, integrated detection systems, suitable for various complex environments. Moreover, BTX gas sensor arrays integrated into the Internet of Things (IoT) network can achieve real-time data transmission and remote monitoring, providing immediate response capabilities for industrial safety and environmental protection. This approach represents a significant advancement in the field, aligning with the trends of digitalization and automation in monitoring systems.

With the rise of nanomaterials and the introduction of advanced electronic processing techniques, chemical resistance gas sensors have made significant progress. However, in the practical application of BTX gas detection, there are still some problems waiting for researchers to solve.

Declaration of competing interest

The authors declare that they have no known competing financial interests or personal relationships that could have appeared to influence the work reported in this paper.

CRediT authorship contribution statement

Yidan Chen: Writing – original draft, Investigation. **Junzhou Xu:** Writing – original draft, Investigation. **Yanjun Pan:** Writing – review & editing, Investigation. **Qi Cao:** Writing – review & editing, Supervision, Funding acquisition, Conceptualization. **Kaiping Yuan:** Writing – review & editing, Supervision.

Acknowledgments

This work was supported by the National Natural Science Foundation of China (Nos. 62104045, 52101213) and Jiangsu Provincial Department of Science and Technology of China (No. BE2022426).

References

[1] D. Shindell, C.J. Smith, Nature 573 (2019) 408–411.
[2] X.Y. Zhang, B. Gao, A.E. Creamer, C.C. Cao, Y.C. Li, J. Hazard. Mater. 338 (2017) 102–123.
[3] Y.C. Wang, Y. Yuan, Q.Y. Wang, et al., Sci. Total Environ. 731 (2020) 139133.
[4] Y. Cheng, H.J. He, C.P. Yang, G.M. Zeng, et al., Biotechnolo. Adv. 34 (2016) 1091–1102.
[5] G. Yadav, A. Singh, A. Dutta, et al., Energy Environ. Sci. 16 (2023) 3638–3653.
[6] R. Fuller, P.J. Landrigan, K. Balakrishnan, et al., Lancet Planet. Heath 6 (2022) E535–E547.
[7] I.C. Dedoussi, S.D. Eastham, E. Monier, S.R.H. Barrett, Nature 578 (2020) 261–265.
[8] F. Chen, G. Zhang, X. Weng, et al., Appl. Catal. A: Gen. 616 (2021) 118095.
[9] F. Goodarzi, D.B. Christensen, F. Joensen, S. Kegnaes, J. Mielby, Appl. Catal. A: Gen. 592 (2020) 117383.
[10] M.J. Kim, J.H. Gong, K.W. Jeon, J.O. Shim, W.J. Jang, Int. J. Hydrogen Energy 49 (2024) 1215–1225.
[11] A. Masih, A.S. Lall, A. Taneja, R. Singhvi, Environ. Pollut. 242 (2018) 1678–1683.
[12] N. Ahmed, Y.S. Ok, B.H. Jeon, et al., Chemosphere 220 (2019) 651–657.
[13] L. Ma, A. Hurtado, S. Eguilior, J.F.L. Borrajo, Sci. Total Environ. 906 (2024) 167638.
[14] K. Dai, C. Wang, W. Yao, C. Hao, Chemosphere 313 (2023) 137460.
[15] A. Mirzaei, J.H. Kim, H.W. Kim, S.S. Kim, J. Mater. Chem. C 6 (2018) 4342–4370.
[16] A. Venkatasubramanian, V.T.K. Sauer, S.K. Roy, et al., Nano Lett. 16 (2016) 6975–6981.
[17] B. Wang, Y.F. Wang, Z. Wang, Z.Y. Hou, ACS Sensors 6 (2021) 908–914.
[18] D.I. Galimov, S.M. Yakupova, K.S. Vasilyuk, R.G. Bulgakov, J. Photoch. Photobio. A 418 (2021) 113430.
[19] C. Wang, Z. Chen, C.L.J. Chan, et al., Nat. Electron. 7 (2024) 157–167.
[20] L. Huang, W. Li, H. Sun, et al., Sensor. Actuat. B: Chem. 399 (2024) 134808.
[21] M.H. Jung, M. Kwak, J. Ahn, et al., ACS Sensors 9 (2024) 217–227.
[22] Z. Liao, Z. Yuan, H. Gao, F. Meng, Sensor. Actuat. B: Chem. 399 (2024) 134815.
[23] S. Zhang, X. Lai, R. Xiao, et al., ACS Sensors 9 (2024) 195–205.
[24] B. Clifford, D. Beynon, C. Phillips, D. Deganello, Sensor. Actuat. B: Chem. 255 (2018) 1031–1038.
[25] S.M. Majhi, A. Mirzaei, H.W. Kim, S.S. Kim, T.W. Kim, Nano Energy 79 (2021) 105369.
[26] A. Mirzaei, H.R. Yousefi, F. Falsafi, et al., Int. J. Hydrogen Energy 44 (2019) 20552–20571.
[27] C. Li, P. Chen, Y. Yu, C. Li, Nanomaterials 12 (2022) 2829.
[28] S.M. Majhi, A. Mirzaei, S. Navale, H.W. Kim, S.S. Kim, Nanoscale 13 (2021) 4728–4757.
[29] M. Yan, J. Tylczak, Y. Yu, G. Panagakos, P. Ohodnicki, Sensor. Actuat. B: Chem. 255 (2018) 357–365.
[30] Y. Tang, Y. Zhoa, H. Liu, ACS Sensors 7 (2022) 3582–3597.
[31] L.X. Ou, M.Y. Liu, L.Y. Zhu, D.W. Zhang, H.L. Lu, Nano-Micro Lett. 14 (2022) 206.
[32] Z. Li, H. Li, Z. Wu, et al., Mater. Horiz. 6 (2019) 470–506.
[33] J. Liu, L. Zhang, J. Fan, J. Yu, Small 18 (2022) 2104984.
[34] S. Ahmed, S.K. Sinha, Environ. Sci. Pollut. Res. 30 (2023) 24975–24986.
[35] J. Ma, Y. Ren, X. Zhou, et al., Adv. Funct. Mater. 28 (2018) 1705268.
[36] J. Wei, D. Zhou, Z. Sun, et al., Adv. Funct. Mater. 23 (2013) 2322–2328.
[37] Y. Jian, W. Hu, Z. Zhao, et al., Nano-Micro Lett. 12 (2020) 71.
[38] M. Lei, M. Gao, X. Yang, et al., ACS Appl. Mater. Interfaces 13 (2021) 51933–51944.
[39] Y.J. Jeong, C. Balamurugan, D.W. Lee, Sensor. Actuat. B: Chem. 229 (2016) 288–296.
[40] M. Tonezzer, Sensor. Actuat. B: Chem. 288 (2019) 53–59.
[41] H. Gao, L. Zhao, L. Wang, et al., Sensor. Actuat. B: Chem. 255 (2018) 3505–3515.
[42] J. Liu, T. Wang, B. Wang, et al., Sensor. Actuat. B: Chem. 245 (2017) 551–559.
[43] H.H. Si, P.N. Huy, H.N. Thanh, N.N. Hoang, H.N. Thi, Appl. Surf. Sci. 492 (2019) 449–454.
[44] S. Sun, M. Wang, X. Chang, et al., Sensor. Actuat. B: Chem. 304 (2020) 127274.
[45] C. Liu, L. Zhao, B. Wang, et al., J. Colloid. Interf. Sci. 495 (2017) 207–215.
[46] F. Meng, L. Qin, H. Guo, H. Zhu, Z. Yuan, Ceram. Int. 50 (2024) 2733–2741.
[47] J. He, X. Yan, A. Liu, et al., J. Mater. Chem. A 7 (2019) 4744–4750.
[48] C. Zhao, J. Shen, S. Xu, et al., Food Chem. 392 (2022) 133318.
[49] A. Gaiardo, G. Zonta, S. Gherardi, et al., Sensors 20 (2020) 5910.
[50] J.B. Liu, J.Y. Hu, C. Liu, et al., Rare Metals 40 (2021) 1536–1544.
[51] H. Hosseinzadehasl, G. Tohidi, F. Movahedi, E. Hassannayebi, J. Saudi Chem. Soc. 25 (2021) 101371.
[52] Z. Li, S. Li, Z. Song, et al., Chemosensors 10 (2022) 327.
[53] L.L. Wang, T.T. Zhou, R. Zhang, et al., Sensor. Actuat. B: Chem. 227 (2016) 448–455.

[54] Q. Yu, X.Q. Gong, Y.R. Jiang, et al., Sensor. Actuat. B: Chem. 372 (2022) 132620.
[55] K.A. Hiyoto, E.R. Fisher, J. Vac. Sci. Technol. A 38 (2020) 043202.
[56] Z.P. Tshabalala, T.P. Mokoena, M. Jozela, et al., ACS Appl. Nano Mater. 4 (2021) 702–716.
[57] S. Hegde, H. Malik, K. Carlson, S.K. Mohanty, K.E. Kelly, IEEE Sens. J. 21 (2021) 13828–13836.
[58] P. Cao, X. Gui, S.T. Navale, et al., J. Alloys Compd. 815 (2020) 152378.
[59] Q. Wang, C. Li, P. Sun, et al., Mater. Res. Express 6 (2019) 1150 e6.
[60] P. Cao, X. Gui, D. Pawar, et al., Mater. Sci. Eng. B 265 (2021) 115031.
[61] K. Karuppasamy, B. Sharma, D. Vikraman, et al., J. Alloys Compd. 886 (2021) 161281.
[62] Y.L. Zhang, C.W. Jia, R.N. Tian, et al., Rare Metals 40 (2020) 1578–1587.
[63] Y. Zhang, Y. Zhou, Z. Li, et al., J. Alloys Compd. 784 (2019) 102–110.
[64] M. Li, W. Xu, R. Jiang, et al., Colloids Surf. A: Physicochem. Eng. Asp. 649 (2022) 129522.
[65] H. Zhang, J. Hu, M. Li, et al., Sensor. Actuat. B: Chem. 349 (2021) 130734.
[66] Z. Cao, Y. Ge, W. Wang, et al., ACS Sensors 7 (2022) 1757–1765.
[67] L. Wang, J.C. Xu, Y.B. Han, et al., Chem. Phys. 560 (2022) 111573.
[68] K. Zhang, P. Tang, Y. Feng, D. Li, Ind. Eng. Chem. Res. 59 (2020) 4472–4482.
[69] H. Gao, D. Wei, P. Lin, et al., Sensor. Actuat. B: Chem. 253 (2017) 1152–1162.
[70] S. Lu, X. Hu, H. Zheng, et al., Sensors 19 (2019) 2958.
[71] C.S. Lee, H.Y. Li, B.Y. Kim, et al., Sensor. Actuat. B: Chem. 285 (2019) 193–200.
[72] H.S. Woo, C.H. Kwak, J.H. Chung, J.H. Lee, Sensor. Actuat. B: Chem. 216 (2015) 358–366.
[73] C. Feng, C. Wang, H. Zhang, et al., Sensor. Actuat. B: Chem. 221 (2015) 1475–1482.
[74] J. Cao, S. Wang, X. Zhao, et al., Mater. Lett. 263 (2020) 127215.
[75] J.G. Thangamani, S.K.K. Pasha, Chemosphere 277 (2021) 130237.
[76] C. Dong, X. Liu, X. Xiao, S. Du, Y. Wang, Sensor. Actuat. B: Chem. 239 (2017) 1231–1236.
[77] R. Zhang, S. Gao, T.T. Zhou, J.C. Tu, T. Zhang, Appl. Surf. Sci. 503 (2020) 144167.
[78] D.H. Kwon, E.H. Jin, D.H. Yoo, et al., Sensors 22 (2022) 4125.
[79] K. Xu, L. Yang, J. Zou, et al., J. Alloys Compd. 706 (2017) 116–125.
[80] Y. Kang, K. Kim, B. Cho, Y. Kwak, J. Kim, ACS Sensors 5 (2020) 754–763.
[81] D. Wang, Y. Cheng, K.C. Wan, et al., Vacuum 179 (2020) 109487.
[82] R. Thangavel, S. Kalainathan, Colloid. Surface. A 686 (2024) 133382.
[83] P. Nagaraju, Y. Vijayakumar, M.V.R. Reddy, J. Asian Ceram. Soc. 7 (2019) 141–146.
[84] J. Cao, S. Wang, J. Li, et al., Sensor. Actuat. B: Chem. 315 (2020) 128120.
[85] F. Li, S. Guo, J. Shen, et al., Sensor. Actuat. B: Chem. 238 (2017) 364–373.
[86] S. Wang, W. Xu, R. Jiang, et al., J. Alloys Compd. 959 (2023) 170569.
[87] M. Zhang, X. Jia, Mater. Lett. 353 (2023) 135297.
[88] T. Zheng, L. Wang, H. Tian, et al., Sensor. Actuat. B: Chem. 339 (2021) 129862.
[89] J. Li, Y. Sun, Z. Tong, et al., New J. Chem. 46 (2022) 14363–14374.
[90] B.X. Feng, Y. Wu, Y. Ren, et al., Sensor. Actuat. B: Chem. 356 (2022) 131358.
[91] M.L. Lei, M.Q. Gao, X.Y. Yang, et al., ACS Appl. Mater. Interfaces 13 (2021) 51933–51944.
[92] S.P.S. David, S. Veeralakshmi, J. Sandhya, S. Nehru, S. Kalaiselvam, Sensor. Actuat. B: Chem. 320 (2020) 128410.
[93] M. Chen, D. Zhang, J. Hu, et al., Mater. Res. Bull. 111 (2019) 320–328.
[94] D. Im, K.B. Park, J.G. Kang, et al., J. Korean Phys. Soc. 74 (2019) 600–606.
[95] S.R. Gottam, C.T. Tsai, L.W. Wang, et al., Appl. Surf. Sci. 506 (2020) 144981.
[96] J.H. Ma, Y.Y. Li, J.C. Li, et al., Adv. Funct. Mater. 32 (2022) 2107439.
[97] X.Y. Yang, Y. Deng, H.T. Yang, et al., Adv. Sci. 10 (2023) 2204810.
[98] J.H. Ma, X.Y. Xiao, Y.D. Zou, et al., Small 15 (2019) 1904240.
[99] J.H. Kim, J.H. Lee, Y. Park, et al., Sensor. Actuat. B: Chem. 294 (2019) 78–88.
[100] S.P.S. David, S. Veeralakshmi, J. Sandhya, S. Nehru, S. Kalaiselvam, Sensor. Actuat. B: Chem. 320 (2020) 128410.
[101] J. Lee, H. Min, Y.S. Choe, et al., Sensor. Actuat. B: Chem. 394 (2023) 134359.
[102] J. Tian, J. Wang, Y. Hao, H. Du, X. Li, Sensor. Actuat. B: Chem. 202 (2014) 795–802.
[103] K. Suematsu, Y. Shin, N. Ma, et al., Anal. Chem. 87 (2015) 8407–8415.
[104] D. Im, K.B. Park, J.G. Kang, et al., J. Korean Phys. Soc. 74 (2019) 600–606.
[105] L.L. Sui, X.F. Zhang, X.L. Cheng, et al., ACS Appl. Mater. Interfaces 9 (2017) 1661–1670.
[106] K.Y. Shin, A. Mirzaei, H.Y. Lee, et al., Sensor. Actuat. B: Chem. 392 (2023) 134049.
[107] C. Wang, S. Zhang, L. Qiu, et al., J. Alloys Compd. 826 (2020) 154196.
[108] C. Zhao, Z. Dong, S. Pan, X. Wu, X. Tang, ACS Appl. Nano Mater. 7 (2024) 15459–15468.
[109] M. Chen, Y. Zhang, J. Zhang, et al., J. Mater. Chem. C 6 (2018) 6138–6145.
[110] M. Chen, Y. Zhang, J. Zhang, et al., Adv. Powder Technol. 34 (2023) 104170.
[111] Y. Shi, M.H. Wang, H.Y. Wang, et al., Mater. Lett. 328 (2022) 133093.
[112] Y. Li, Q. Zhou, S. Ding, Z. Wu, Front. Chem. 9 (2021) 786607.
[113] W. Xu, C. Qiu, J. Zhou, Y. Chen, Ceram. Int. 46 (2020) 11372–11378.
[114] C. Zhai, M. Zhu, L. Jiang, et al., Appl. Surf. Sci. 463 (2019) 1078–1084.
[115] S.X.L. Luo, C.J. Lin, K.H. Ku, K. Yoshinaga, T.M. Swager, ACS Nano 14 (2020) 7297–7307.
[116] C.J. Arockiam, R. Ananthanarayanan, P. Srinivasan, A. Krishnakumar, Mater. Sci. Semicond. Process. 132 (2021) 105930.
[117] D. Wang, Y. Yin, P. Xu, et al., J. Mater. Chem. A 8 (2020) 11188–11194.
[118] W. Wang, F. Li, N. Zhang, et al., Sensor. Actuat. B: Chem. 351 (2022) 130931.
[119] S. Dey, S. Santra, S.K. Ray, P.K. Guha, IEEE Sens. J. 20 (2020) 7503–7508.
[120] H. Liu, Z. Wang, G. Cao, et al., Mater. Sci. Semicond. Process. 141 (2022) 106435.
[121] A. Hermawan, Y. Asakura, M. Inada, S. Yin, J. Mater. Sci. Technol. 51 (2020) 119–129.
[122] T. Liu, Z. Yu, Y. Liu, et al., Sensor. Actuat. B: Chem. 318 (2020) 128167.
[123] H. Chen, S. Ao, G.D. Li, et al., Sensor. Actuat. B: Chem. 282 (2019) 331–338.
[124] L. Nie, G. Fan, A. Wang, et al., Sensor. Actuat. B: Chem. 345 (2021) 130412.
[125] Z. Cai, J. Park, S. Park, J. Mater. Res. Technol. 24 (2023) 2482–2499.
[126] J.H. Kim, H.M. Jeong, C.W. Na, et al., Sensor. Actuat. B: Chem. 235 (2016) 498–506.
[127] J. Guo, Y. Li, B. Jiang, et al., Sensor. Actuat. B: Chem. 310 (2020) 127780.
[128] F. Qu, S. Zhang, B. Zhang, et al., Microchim. Acta 186 (2019) 222.
[129] M. Guo, N. Luo, Y. Chen, et al., J. Hazard. Mater. 429 (2022) 127471.
[130] F. Qu, X. Zhou, B. Zhang, et al., J. Alloys Compd. 782 (2019) 672–678.
[131] D.Y. Wang, Q. Mi, H. Zhang, G.L. Li, D.Z. Zhang, IEEE Sens. J. 22 (2022) 10346–10352.
[132] H. Gao, J. Guo, Y. Li, et al., Sensor. Actuat. B: Chem. 284 (2019) 305–315.
[133] H. Wang, M. Chen, Q. Rong, et al., Nanotechnology 31 (2020) 255501.
[134] R. Makole, Z.P. Tshabalala, M. Jozela, et al., Inorg. Chem. Commun. 158 (2023) 111652.
[135] L. Qin, H. Gao, F. Meng, Chemosensors 11 (2023) 264.
[136] L.M. Maebana, R.G. Motsoeneng, Z.P. Tshabalala, et al., J. Alloys Compd. 960 (2023) 170683.
[137] H. Gao, Q. Yu, K. Chen, et al., J. Colloid. Interf. Sci. 535 (2019) 458–468.
[138] J.H. Kim, J.H. Lee, A. Mirzaei, H.W. Kim, S.S. Kim, Sensor. Actuat. B: Chem. 248 (2017) 500–511.
[139] Y. Kang, K. Kim, B. Cho, Y. Kwak, J. Kim, ACS Sensor 5 (2024) 754–763.
[140] S. Behi, N. Bohli, J. Casanova-Cháfer, E. Llobet, A. Abdelghani, Sensors 20 (2020) 3413.
[141] G.S. Aluri, A. Motayed, A.V. Davydov, et al., Nanotechnology 22 (2011) 295503.
[142] W. Guo, Q. Zhou, J. Zhang, et al., Sensor. Actuat. B: Chem. 299 (2019) 126959.
[143] Q. Feng, H. Zhang, Y. Shi, X. Yu, G. Lan, Polymers 13 (2021) 1360.
[144] S.Paul Choudhury, Z. Feng, C. Gao, et al., J. Alloys Compd. 815 (2020) 152376.
[145] A. Hermawan, B. Zhang, A. Taufik, et al., ACS Appl. Nano Mater. 3 (2020) 4755–4766.
[146] S. Srivastava, A. Singh, M. Sahz, B.C. Yadav, N.K. Pandey, Sensor. Actuat. B: Chem. 400 (2024) 134817.
[147] P. Yadav, A.K. Sharma, S.K. Yadav, A.K. Vishwakarma, L. Yadava, Mater. Today: Proc. 38 (2020) 2792–2796.
[148] Y. Zhang, C. Jia, Q. Wang, et al., Ind. Eng. Chem. Res. 58 (2019) 9450–9457.
[149] L. Hu, F. Jia, S. Wang, et al., J. Mater. Sci. 56 (2020) 5041–5052.
[150] M. Ran, Z. Yuan, H. Zhu, H. Gao, F. Meng, Chemosensors 11 (2023) 568.
[151] K.Y. Choi, J.S. Park, K.B. Park, et al., Sensor. Actuat. B: Chem. 150 (2010) 65–72.
[152] F. Meng, X. Li, Z. Yuan, et al., IEEE Trans. Instrum. Meas. 70 (2021) 1–10.
[153] S. Jung, R. Hauert, M. Haluska, C. Roman, C. Hierold, Sensor. Actuat. B: Chem. 331 (2020) 129406.
[154] F. Liu, M. Xiao, Y. Ning, et al., Sci. China Inform. Sci. 65 (2022) 162402.
[155] G. Peng, S. Wu, J.E. Ellis, et al., J. Mater. Chem. C 4 (2016) 6575.
[156] L. Xue, W. Wang, Y. Guo, G. Liu, P. Wan, Sensor. Actuat. B: Chem. 244 (2016) 47–53.
[157] H. Onthath, M.R. Maurya, S. Bykkam, et al., Macromol. Symp. 400 (2021) 2100202.
[158] Y.S. Kang, K. Kim, B. Cho, Y.J. Kwak, J.B. Kim, ACS Sensor 5 (2020) 754–763.
[159] B. Cho, J. Yoon, S.K. Lim, et al., ACS Appl. Mater. Interfaces 7 (2015) 16775–16780.
[160] W. Quan, J. Shi, H. Luo, et al., ACS Sensors 8 (2023) 103–113.
[161] E. Singh, M. Meyyappan, H.S. Nalwa, ACS Appl. Mater. Interfaces 9 (2017) 34544–34586.
[162] H. Tai, Z. Duan, Y. Wang, S. Wang, Y. Jiang, ACS Appl. Mater. Interfaces 12 (2020) 31037–31053.
[163] Z. Wu, H. Wang, Q. Ding, et al., Adv. Funct. Mater. 33 (2023) 2300046.
[164] J. Gao, L. Wang, Z. Guo, et al., Chem. Eng. J. 381 (2020) 122778.
[165] X. Liu, W. Zheng, R. Kumar, M. Kumar, J. Zhang, Coord. Chem. Rev. 462 (2022) 214517.
[166] Y. Seekaew, S. Lokavee, D. Phokharatkul, et al., Org. Electron. 15 (2014) 2971–2981.
[167] P.J. Maake, T.P. Mokoena, A.S. Bolokang, et al., Mater. Adv. 3 (2022) 7302–7318.
[168] X. Liu, X. Duan, C. Zhang, P. Hou, X. Xu, J. Alloys Compd. 897 (2022) 163222.
[169] Y. Sun, Z. Zhao, K. Suematsu, et al., Sensor. Actuat. B: Chem. 360 (2022) 131631.
[170] J.H. Kim, H.W. Kim, S.S. Kim, Sensor. Actuat. B: Chem. 251 (2017) 781–794.
[171] Y. Lu, J. Zhang, W. Wang, et al., Sensor. Actuat. B: Chem. 351 (2022) 130907.
[172] T. Akiyama, Y. Ishikawa, K. Hara, Sensor. Actuat. B: Chem. 181 (2013) 348–352.
[173] V. Chaudhary, S.P. Nehra, Micropor. Mesopor. Mater. 315 (2021) 110906.
[174] Z.U. Abideen, J.H. Kim, A. Mirzaei, H.W. Kim, S.S. Kim, Sensor. Actuat. B: Chem. 255 (2018) 1884–1896.
[175] V.S. Bhati, M. Hojamberdiev, M. Kumar, Energy Rep. 6 (2020) 46–62.
[176] L. He, Y. Liu, J. Liu, et al., Angew. Chem. Int. Ed. 52 (2013) 3741–3745.
[177] J. Lee, Y. Jung, S.H. Sung, et al., J. Mater. Chem. A 9 (2021) 1159–1167.
[178] Y. Luo, C. Zhang, B. Zheng, X. Geng, M. Debliquy, Int. J. Hydrogen Energy 42 (2017) 20386–20397.
[179] J.H. Kim, A. Mirzaei, H.W. Kim, S.S. Kim, Sensor. Actuat. A: Phys. 308 (2020) 112011.
[180] D. Gulevich, M. Rumyantseva, E. Gerasimov, et al., Nanomaterials 10 (2020) 813.

[181] Y.J. Kwon, S.W. Choi, S.Y. Kang, et al., Sensor. Actuat. B: Chem. 244 (2017) 1085–1097.
[182] M. Bonyani, J.K. Lee, G.J. Sun, et al., Thin Solid Films 636 (2017) 257–266.
[183] Z. Wang, H. Liu, J. Shao, et al., Nanotechnology 33 (2022) 365501.
[184] C. Gong, M. Chen, F. Song, et al., ACS Appl. Electron. Mater. 6 (2024) 6036–6048.
[185] J.H. Bang, M.S. Choi, A. Mirzaei, et al., Appl. Surf. Sci. 525 (2020) 146620.
[186] M.G. Campbell, S.F. Liu, T.M. Swager, M. Dinca, J. Am. Chem. Soc. 137 (2015) 13780–13783.
[187] W.T. Koo, J.S. Jang, I.D. Kim, Chem 5 (2019) 1938–1963.
[188] H.Y. Li, S.N. Zhao, S.Q. Zang, J. Li, Chem. Soc. Rev. 49 (2020) 6364–6401.
[189] Z. Song, Z. Wei, B. Wang, et al., Chem. Mater. 28 (2016) 1205–1212.
[190] M.S. Yao, X.J. Lv, Z.H. Fu, et al., Angew. Chem. Int. Ed. 56 (2017) 16510–16514.
[191] Y. Zhang, S. Han, M.Y. Wang, et al., J. Adv. Ceram. 11 (2022) 427–442.
[192] H. Wang, Z. Sun, Q. Lu, F. Zeng, D. Su, Small 8 (2012) 1167–1172.
[193] M. Yan, K. Liang, D. Zhao, B. Kong, Small 18 (2021) 2102887.
[194] H.Y. Yuan, S. Aljneibi, J.R. Yuan, et al., Adv. Mater. 31 (2019) 1807161.
[195] K. Lan, Q. Wei, D. Zhao, Angew. Chem. Int. Ed. 61 (2022) e202200777.
[196] Y. Ai, W. Li, D. Zhao, Natl. Sci. Rev. 9 (2021) nwab108.
[197] Q. Feng, B. Huang, X. Li, Adv. Funct. Mater. 31 (2021) 2104058.
[198] L. Zhang, S. Zhang, C. Huang, et al., J. Alloys Compd. 862 (2021) 158489.
[199] M. Yi, M. Jing, Y. Yang, et al., Adv. Funct. Mater. 34 (2024) 2400001.
[200] T. Wu, M. Jing, L. Yang, et al., Adv. Energy Mater. 9 (2019) 1803478.
[201] Q. Cao, J. Zhang, H.B. Zhang, J.Z. Xu, R.C. Che, J. Adv. Ceram. 11 (2022) 504–514.
[202] M. Liu, X.P. Duan, Y.M. Li, D.P. Yang, Y.Z. Long, Mat. Sci. Eng. C 76 (2017) 1413–1423.
[203] X. Lu, C. Wang, F. Favier, N. Pinna, Adv. Energy Mater. 7 (2017) 1601301.
[204] C. Dimitriou, P. Psathas, M. Solakidou, Y. Deligiannakis, Nanomaterials 13 (2023) 3006.
[205] S. Venkatesan, J. Mitzel, K. Wegner, et al., Renew. Sust. Energ. Rev. 158 (2022) 112080.
[206] Y. Ishida, R.D. Corpuz, T. Yonezawa, Acc. Chem. Res. 50 (2017) 2986–2995.
[207] L. Peng, H. Peng, W. Li, D. Zhao, Nat. Protoco. 18 (2022) 1155–1178.
[208] T. Zhao, A. Elzatahry, X. Li, D. Zhao, Nat. Rev. Mater. 4 (2019) 775–791.